Spatial transcriptomics reveals recasting of signalling networks in the small intestine following tissue invasion by the helminth parasite *Heligmosomoides polygyrus*

Marta Campillo Poveda*[§], Olympia Hardy[§], Ross F Laidlaw[§,†], Thomas D Otto, Rick M Maizels*

Centre for Parasitology, School of Infection and Immunity, University of Glasgow, UK

† Current Address : Leiden University Medical Center, The Netherlands

[§] These authors made equal contributions to the manuscript.

* Corresponding Authors: Marta Campillo Poveda, marta.campillopoveda@glasgow.ac.uk and Rick Maizels, rick.maizels@glasgow.ac.uk

Abstract

The infective larvae of the helminth *Heligmosomoides polygyrus bakeri* migrate to the small intestine, invade the submucosa, and trigger granuloma formation around each parasite. Here, we employ spatial transcriptomics to elucidate the transcriptional intricacies and cell interactions in *H. polygyrus*-infected mice. We find a generalised reduction in expression of homeostatic genes such as *Epcam*, *Pls1* (fimbrin) and *Zg16*, while cell adhesion (eg *Cldn3*, *Cdh17*) and immune-protective (*Pla2g4c*) loci are upregulated. Specific genes and cell types are associated with different spatial niches (lower crypt, upper crypt, villi and granuloma). Within the crypts, pathway analysis indicates activation of the osteopontin (*Spp1*) and pleiotrophin (*Ptn*) pathways that are poorly represented in steady-state tissues, whilst *Wnt* signalling within the crypts is abrogated by day 7 of infection. Granulomas contain concentrations of myeloid cells, NK and dendritic cells, with high expression levels of genes linked to M2 macrophages (*Arg1*, *Retlna*, *Fcer1g*) and wound repair pathways (*Reg3b* and *Mxra7*) as well as elevated *Tmbx4* that has not previously been noted. Analysis of potential ligand-receptor pairs confirmed a major complementarity between granuloma-localised SPP1 and CD44 receptors in both crypt and granuloma, as well as TGF-β/receptor interactions. Infected tissues also revealed abundant chemokine representation; among the latter category CCL6, CCL8 and MIF (macrophage migration inhibitory factor) dominated potential interactions. These results both enhance our understanding of the murine small intestine's transcriptional landscape and also identify a new set of molecular interactions underpinning tissue-specific responses to infection that can be targeted for therapeutic intervention.

33 **1. Introduction**

34 Helminths, or parasitic worms, are amongst the most prevalent infectious agents
35 afflicting individuals in developing nations, contributing to a global disease burden as
36 severe as more recognized conditions like malaria and tuberculosis. Most helminth
37 infections establish long-lived chronic parasitism, exacerbating the global health
38 problem, and causing extensive morbidity in both humans [1] and livestock [2]. A widely
39 used model for intestinal helminth infections is *Heligmosomoides polygyrus bakeri*, a
40 natural parasite of mice that can persist for many weeks or months in laboratory strains,
41 defying the host's attempts to mount an effective immune response [3, 4].

42 Intestinal helminth infections present especial challenges when parasites, such as *H.*
43 *polygyrus*, invade the submucosal tissues; here the concerted efforts of macrophages
44 and granulocytes play a pivotal role in defence against invading parasites [5-10]. Upon oral
45 ingestion, *H. polygyrus* larvae swiftly traverse the small intestine's epithelial barrier,
46 establishing in the submucosal tissue before maturing into adults and returning to the
47 intestinal lumen 7-8 days later. Infection initiates a dominant type 2 immune response
48 [6, 11], alongside an expansion of regulatory T cells [12-14] and early IFN-γ production [15, 16].
49 Together these orchestrate crucial physiological processes, ranging from parasite
50 containment [17], epithelial differentiation [15, 18], and restoration of barrier integrity [19, 20].
51 The extensive localised and systemic properties of these responses highlight the
52 recruitment of both "professional immune" and nonhaematopoietic cells into the type
53 2 effector orbit [21], with the larvae rapidly encased in a granuloma surrounded and
54 infiltrated by macrophages, neutrophils, and eosinophils, among other cell types [5, 22]. In
55 contrast to type 1 intestinal granulomas elicited by bacterial infection through TNF and
56 IL-1 [23], *H. polygyrus* granulomas are driven by type 2 cytokines and are more extensive
57 in IL-1R-deficient mice [24]. A type 2 effector network forms in the infected tissue, with
58 mast cells contributing to type 2 innate lymphoid cell (ILC2) activation [25], upstream of
59 Th2 differentiation [26], and eosinophils stimulating neuroprotective macrophages [27]
60 while type 2 cytokines drive smooth muscle hyperreactivity and increased epithelial
61 permeability [10].

62 Despite the host's robust immune response, *H. polygyrus* establishes long-term chronic
63 infections attributed to its immunomodulatory effects. Most notable is its secretion of
64 proteins that mimic the function of TGF-β [28, 29], a pivotal regulator of the immune system
65 through the induction of T regulatory cells, which inhibit the inflammatory effects of a
66 variety of immune cells [30, 31]. Until recently, investigations into helminth immuno-
67 modulation predominantly focused on its downstream impacts on immune cell
68 populations. However, increasing attention is being paid to the complex interactions
69 between intestinal helminths and the epithelium [15, 18, 32]. Particularly noteworthy are
70 findings from the early stages of *H. polygyrus* infection, in which localised cysts or
71 granulomas, typically 500-900 µm in size, form around each individual larva. During this
72 phase, stem cells in the surrounding crypts have been observed to undergo a "reversal"
73 to a foetal-like repair phenotype [15]. Additionally, these stem cells exhibit a compromised
74 capacity to differentiate into various effector secretory cell subsets, including tuft,
75 goblet, and Paneth cells [15, 18, 32], a finding that can be recapitulated in organoid cultures
76 of intestinal stem cells exposed to *H. polygyrus* or its secreted products [18].

77 While the interactions and effects of the nematode on the immune system and
78 epithelium are clearly extensive, it is important to better understand the spatial context
79 in which host-parasite interactions occur and to identify changes occurring across
80 infected tissues that may determine parasite establishment or clearance. In recent
81 years, a powerful new set of techniques that combine transcriptomics with histology
82 has emerged under the "Spatial Transcriptomics" umbrella. This technology assesses
83 gene transcription in individual cells or tissues using spatial resolution of <100 µm,
84 accompanied by high-dimensional data collection. The visualisation and quantitative
85 analysis of gene expression in tissue sections offers multiple insights into cell-to-cell
86 interactions, tissue heterogeneity, and functional organisation [33-35], making it an
87 impressively powerful tool to analyse the mechanistic basis of host-parasite
88 interactions.

89 In this study, spatial transcriptomics were employed to investigate the localised
90 transcriptional profile within the intestinal epithelium and lamina propria of both naïve
91 mice and mice infected with *H. polygyrus* over the first 7 days of infection. This has
92 allowed us to pinpoint immune cell types within the granuloma, and identify potential

93 ligand-receptor pairs mediating communication between tissue sites in granuloma
94 formation and stem cell differentiation. Notably, our investigation unveiled a suite of
95 transcriptional and morphological changes extending beyond conventional immune
96 responses, providing new insights into the complex interplay between *H. polygyrus* and
97 the intestinal environment and how the intestinal tissue is reorganised in response to
98 parasite invasion.

99 **2. Results**

100 *2.1. Spatial transcriptomics confirms distinct steady state transcriptional signatures*
101 *associated with different regions of the murine small intestine*

102 When infective L3 larvae of *H. polygyrus* are ingested and migrate to the small intestine,
103 they cross the epithelial barrier and take up residence in the submucosa for 8 days
104 before returning to the lumen [4]. To profile the transcriptomic landscape of the small
105 intestine tissue, we employed the Visium (10X Genomics) platform to conduct spatial
106 transcriptomics on formalin-fixed gut tissue, sectioned from a Swiss roll preparation
107 (Fig. 1 A) from *H. polygyrus*-infected mice at days 3, 5 and 7 post-infection. We focused
108 on the two fundamental categories of the small intestine, the crypt zone (including the
109 lamina propria and the crypts) and the villi; an additional category in *H. polygyrus*-
110 infected mice are the inflammatory granulomas forming around individual larvae within
111 the submucosa (Fig. 1 B) which form immediately adjacent to the crypts (Fig. 1 C) and
112 as previously reported [5] are rich in Type-2 macrophages expressing Arginase-1 (Fig. 1
113 D).

114 We first examined naïve intestinal tissue, analysing a total of 4992 spots which were
115 analysed and manually assigned a category, using the Loupe Browser (10X Genomics).
116 The dataset was filtered by removing spots that were not unambiguously labelled and
117 removing genes that had expression in 3 or fewer spots. This processed dataset from
118 naïve mice contained expression values from 3560 valid spots across 19465 genes which
119 had, on average, 32087 unique molecular identifiers (UMI) per spot.

120 The presence of known cell-specific transcriptomic markers was found to be consistent
121 with the assigned spatial categories, with distinct sets of crypt-associated and villus-

122 associated gene expression (Supp. Fig. 1 A). Genes such as the intestinal stem cell
123 marker *Smoc2* [36] (Supp. Fig. 1 B) and growth regulator *Rack1* [37] define the crypt zone,
124 where the stem cells differentiate, and developing epithelial cells start to express
125 markers of specialisation. On the other hand, the hallmark villus signature is the villin
126 gene *Vil1* [38] (Supp. Fig. 1 C). Other genes preferentially expressed by villi include the
127 cytoskeletal components *Ezr* (Ezrin/Villin-2), *Myo15b* (myosin XVB) and *Pls1*
128 *(Pastin1/*fimbrin), and class II major histocompatibility complex (MHC II) genes *H2-Q1*
129 and *H2-Q2*, which help maintain the tight junctions of the enterocytes and facilitate the
130 presentation of antigens respectively [39].

131 *2.2 Spatial transcriptomics reveals early shift in Wnt signalling following* H. polygyrus
132 *infection.*

133 We next investigated temporal shifts in signalling pathways, particularly within the crypt
134 microenvironment at days 3, 5 and 7 following *H. polygyrus* infection, revealing
135 extensive shifts in gene expression that are differentially regulated, with up to 700
136 significant changes comparing two time points (Fig. 2 A) with numerous genes
137 prominent at each day evaluated (Fig. 2 B, Suppl. Fig 2). These changes result in a similar
138 pattern of gene expressions on days 3 and 7 compared to naïve and day 5 (Fig. 2 B). This
139 shift matches parasite's life cycle events: around days 3 and 7 epithelial barrier breach
140 and tissue penetration occurs, while Naïve and Day 5 represent the steady state and the
141 period while the parasite is encapsulated inside the granuloma. Pathway analysis was
142 then applied to identify key functional gene sets that are influenced during infection
143 (Fig. 2 C). Global immune cell genes associated with CD45 became increasingly
144 prominent over the course of infection, coinciding with the immune cell influx
145 characteristic of early granuloma formation, where monocytes, neutrophils, and
146 eosinophils begin surrounding the parasite [5, 17]. Notably, increased expression of Ccl
147 chemokines (*Ccl6, Ccl7, Ccl8*) was observed at later time points, suggesting a sustained
148 immune recruitment process (Fig. 2 C). Given that *H. polygyrus* larvae are still developing
149 in the submucosa at this stage, chemokine upregulation may reflect a continued attempt
150 by the host to mount an effective immune response, while the parasite simultaneously
151 suppresses more direct effector mechanisms [8].

By day 7, additional signalling pathways associated with tissue remodelling became dominant, including TGF-β (*Tgfb1*), osteopontin (*Spp1*), and thrombospondins (Fig. 2 C). These factors have been implicated in fibrosis and extracellular matrix remodelling in chronic helminth infections, potentially facilitating wound healing while also reinforcing a permissive niche for parasite persistence [28, 40]. In contrast, we noted a complete loss of Wnt pathway genes from the expression profile by day 7 post-infection (Fig. 2 C).

In naïve mice, crypt-to-crypt interactions were dominated by Wnt signalling, consistent with its role in maintaining intestinal stem cell proliferation and epithelial homeostasis [15, 41]. This aligns with previous reports showing that in the absence of infection, Wnt-driven differentiation sustains normal epithelial renewal, balancing secretory and absorptive cell lineages [42]. When we examined individual Wnt pathway members, a marked reduction in their expression levels was already evident by day 3 (Fig. 2 D, E). By day 7 post-infection, Wnt gene expression was almost completely absent, while Notch signalling was strongly upregulated, indicating a shift towards an absorptive lineage bias. This mirrors findings from *H. polygyrus*-infected organoid cultures, where parasite-secreted products suppress secretory cell differentiation, favouring a foetal-like repair phenotype [18].

2.3 Crypts and villi show distinct perturbations in expression profiles

We then focussed on gene expression in tissues taken 7 days post-*H. polygyrus* infection. In the infected sample, as with naïve mice described above, each spot was assigned a category by hand, using the Loupe Browser (10X Genomics), with the additional category of granuloma. Filtering of the sample was carried out in a similar fashion to the naïve, with the resulting dataset having 3964 valid spots across 19465 genes, and a mean UMI count of 10077 per spot.

When combining the overall transcriptional datasets irrespective of infection status we observed a clear division of the spots assigned to the different categories, separating the crypt zones and the villi in both naïve (Fig. 3 A) and day 7-infected (Fig. 3 B) mice, with the latter also displaying prominent granulomas. Next, when the two datasets are integrated, we found a clear separation between naïve and infected samples (Fig. 3 C).

181 The latter finding underscores the profound transformation of gene expression in the
182 small intestine following *H. polygyrus* infection in mice.

183 We then focussed separately on the crypt and villous areas of the small intestine in naïve
184 and infected murine tissues and identified specific genetic signatures in each of the
185 tissue niches during infection (Fig. 3 D). Specifically, after 7 days of infection, crypts show
186 ablated expression of genes associated with intestinal homeostasis like *Zg16*, *Muc13,*
187 *Itln1* and *Fcgbp*, which help protect the intestine against bacterial colonisation [43-45] (Fig.
188 3 E, Suppl. Fig. 3 A). In the infected crypts there is also a reduction in factors that
189 maintain the integrity of the intestinal barrier such as *Epcam* and *Pls1* [46].

190 On the other hand, a different suite of genes is upregulated in the infected crypts (Fig. 3
191 F, Suppl. Fig. 3 A), with most elevated expression of cell adhesion proteins (*Cldn3*, *Cdh17*)
192 [47, 48] which may signify epithelial cell proliferation and modification in tight junctions at
193 this early stage of infection. A marked induction is seen of the phospholipase A2 family
194 member *Pla2g4c,* which is involved in and required for killing of larval *H. polygyrus* [49]. A
195 further induction from a low basal level is seen with the pyroptosis associated factor
196 *Gsdmc4* (Suppl. Fig. 3 A), which is known to be upregulated in IL-4 treated and
197 *Nippostrongylus brasiliensis* infected mouse intestinal cells [50].

198 Within the villi tissues, a similar reduction in expression profile is seen for pro-
199 homeostatic genes such as *Epcam*, but distinct from crypt cells, the villi show down-
200 regulation of metabolic mediators such as the mitochondrial ATP translocase *Slc25a5*,
201 and the dipeptidase *Cndp2* (Fig. 3 , Suppl. Fig. 3 B), while upregulating *Cldn3* and *Pla2g4c*
202 as observed for crypt tissues (Fig. 3 H, Suppl. Fig. 3 B).

203 We also examined expression of a gene set associated with epithelial cell differentiation
204 (*Atoh1, Gfi1, HES1* and *Neurog3*), goblet cell expression (*Clca1, Muc2*) and tuft cell
205 function (*Alox5, Hgpds and Ptgs1*), as earlier *in vitro* studies had reported modulation in
206 organoids treated with *H. polygyrus* products [18]. However, while *Clca1, Hes1* and *Muc2*
207 were reduced in infected crypts, most other gene transcripts were expressed at too low
208 a level to be conclusive (Suppl. Fig. 3 C); a similar profile of low transcript levels apart
209 from the same 3 genes was found In the analysis of villi (Suppl. Fig. 3 D).

210 *2.4 Molecular characterization of the* H. polygyrus *granuloma and the surrounding small*
211 *intestine.*

212 Next, we focused on the post-infection granulomas surrounding larval parasites in the
213 submucosal tissue (Fig. 1 B-D), of which 10 distinct sites were identified (Suppl. Fig. 4
214 A). We compared the combined transcriptomic signatures of all granulomas in
215 comparison to the rest of the intestinal tissue (Fig. 4 A). Remarkably, we found high
216 expression of *Tmsb4x*, encoding thymosin beta-4, a small protein that may promote
217 dendritic cell differentiation [51]. As previously noted, *Arg1* (arginase-1) is highly
218 expressed in the granulomas [5], as is *Retnla* (encoding RELM-α), and both genes are
219 closely associated with alternatively activated (M2) macrophages; the marked elevation
220 of *Ccl8* (the chemokine CCL8/monocyte chemoattractant protein-2) and *Ccl9*
221 (CCL9/macrophage inflammatory protein 1-γ) is consistent with dominant infiltration
222 by macrophages. Similarly, *Fcer1g,* the IgE receptor, has previously been linked to
223 macrophages in multiple tumour and inflammatory settings, with a general activating
224 role. Additional upregulated genes are involved in extracellular matrix (ECM) deposition
225 (*Fn1*, *Col1a1*, and *Ctsb*) as well as antigen presentation and immune stimulation (*C1qa*,
226 *Tnfaip2*), and lipid metabolism and oxidative stress regulation (*Apoe, Cyba, Psap*) [52, 53].
227 These upregulated genes collectively imply a coordinated response involving myeloid
228 immune cells, tissue repair, and activation of inflammatory and remodelling processes
229 within the granuloma microenvironment.

230 A further comparison was then made between granulomas and the crypt sites,
231 excluding other epithelial tissues. This analysis, presented as a volcano plot in Fig. 4 B,
232 confirms the high levels of *Arg1* and *Retnla*, as well as the monocyte chemoattractants
233 *Ccl8* and *Basp1*. In contrast, there is concomitant *downregulation* of defensins and
234 *Zbtb48*. The local concentration of these products was confirmed by a spatial analysis
235 of expression relative to distance from the site of the granuloma (Fig. 4 C), and by
236 mapping expression of transcripts for *Arg1* (Fig. 4 D), *Basp1* (Fig. 4 E) and *Lgals1* (Fig. 4
237 F) onto the overall landscape.

238 We then turned to the question of heterogeneity within the set of granulomas, which
239 differed in their presentation, and were transcriptionally variable as shown by UMAP

240 analysis (Suppl. Fig. 4 B), which resolved into three distinct clusters (Fig. 4 G, H). Cluster
241 0 spots represent granulomas in which no larva is visible, either because the adult is
242 already in the lumen or because the section is offset with respect to the worm (Fig. 4 I,
243 Suppl. Fig 4 C). Analysis of differential gene expression by the 3 clusters (Fig. 4 J, Suppl.
244 Fig. 4 D), reveals interesting profiles of specific gene sets. In Cluster 0, there is a higher
245 level of immune cell products including the MHC Class II antigen *H2-Q2*, and proteins
246 involved in interferon responses (*Ifi27l2b*), and immune regulation (*Clec2h*).
247 Furthermore, the upregulation of *Vil1*, *Zg16*, and *Krt20* suggests the presence of
248 epithelial cells that may contribute to the structure within the granuloma [54].
249 Interestingly, one of the upregulated genes of cluster 0 granulomas is *Zg16*, which is
250 conversely down-regulated in infected villi (Fig. 4 G, Fig. 4 J).

251 The observed gene expression within Cluster 1 of granulomas containing larval parasites
252 encompasses features of both type 1 and type 2 immunity. The upregulation of pro-
253 inflammatory genes such as M cell products *Tnfaip2* and *Ccl9* [55] and IgE receptor *Fcer1g*
254 [56] is observed alongside genes such as *Arg1*, *Basp1*, *C1qa*, *Fn1*, *Emilin1*, and *Psap* [57-60]
255 which point towards M2 macrophage activation and associated angiogenesis, tissue
256 repair and extracellular matrix remodelling (Fig. 4 J).

257 Cluster 2, which represents a single granuloma which like Cluster 0 has no visible larva
258 (Fig. 4 J and Suppl. Fig. 4), but shows a very distinctive gene profile with a lower level of
259 macrophage activation genes, compensated by higher *Reg3b, Reg3g* and *Agr2*
260 expression indicating resolution and regeneration of the cellular environment [34, 61, 62],
261 together with *Mxra7*, encoding Matrix remodelling associated 7 protein implicated in
262 wound-healing [63]. Additionally, a suite of histone genes (*Hist1h4h, Hist1h1c, Hist1h3c*)
263 [64], RNA processing and translation-related genes (*Eef1a1, Eef1b2, Pcbp2, Pdcd4, Rbm5,*
264 *Sf3b1*), and genes associated with protein quality control suggest reinvigorated
265 metabolic activity [65-67] and recovery from stress [68, 69] (Fig. 4 J) .

266 *2.5 Gene expression perturbations in tissues proximal to larval sites*

267 In addition to defining gene expression patterns within the granulomas, we asked
268 whether intestinal crypts adjacent to, or distant from, the sites of larval establishment

showed differential transcriptional profiles. We classified sets of crypts in each category (Fig. 5 A) and identified gene sets that were up- or down-regulated in proximal sites, as candidate genes that are modulated by the presence of the helminth larvae (Fig. 5 B, C). A number of genes upregulated in the vicinity of granulomas are macrophage-associated products also found within the granulomas such as *Retnla* and *Fcer1g*, although *Arg1* was not highlighted. Of particular interest however, we noted that 2 components of the Wnt pathway, *Dact2* and *Frat2* are locally down-regulated, consistent with the overall reduction in Wnt signalling.

2.6 Cellular composition of tissue niches

Having recreated the original biological spatial context of the intestine, we next identified the cell types present and their distribution across the spatial axis. In bulk RNA-seq data cell type abundance can be estimated by cell type deconvolution, where a scRNA-seq reference dataset is used to estimate the proportions of different cell types within a bulk sample [70]. To deconvolute the Visium spot data, we used cell2location [71], a method for deconvoluting spatial transcriptomic data which builds expression profiles of cell types from a reference scRNA-seq dataset and uses these profiles to decompose the transcripts within spots into the supplied cell types from the scRNA-seq dataset.

We integrated two scRNA-seq datasets of immune and non-immune cells from the intestines of mice respectively from published studies [72, 73] to ensure there would be sufficient representation of the immune and epithelial cell types that comprise the intestine. Leveraging these annotations, we focused on the most proximal part of the intestine, the duodenum, which is the primary site of *H. polygyrus* tissue invasion and luminal occupancy (Fig. 6 A). Ensuring that we preserved spatial localisation of the tissue we used our calculated spatial embeddings containing our unrolled length (anterior to posterior, Fig. 6 B) and depth (lower crypt to villous tip) (Fig. 6 C) axes, and the original Visium spatial coordinates, to ensure adjacent segments in the Visium space are separated from each other (Fig. 6 D). After applying non-negative matrix factorization (see Methods) to identify which cell types colocalize together in the same spatial niches, noting that in both naïve and *H. polygyrus* infected mouse intestine, there are common signatures of cell type colocalization, especially among the non-immune cells.

299 Within the deepest spot layer of the crypts in both naïve and infected mice, the Lower
300 Crypt spatial niche is dominated by transit amplifying (TA) cells and intestinal stem cells,
301 with the presence of both $CD4^+$ and $CD8^+$ T cell subsets (Fig. 6 E, F, Suppl. Fig. 5 A).
302 Directly above, the Upper Crypt is almost entirely composed of enterocyte progenitors
303 with minor representation of lymphoid cells (Fig. 6 E, F, Suppl. Fig. 5 A). Extending
304 toward the lumen, the villous niche colocalises enterocytes, B cells, innate lymphoid
305 cells (ILC) 1 and 2, NK cells and γδ T cells (Fig. 6 E, F, Suppl. Fig. 5 A).

306 Focusing on colocalization signatures that are specific to infected mice, an accumulation
307 of macrophage, neutrophil, plasmacytoid DC, mast cell and lymphoid tissue inducer
308 cells localised in the intestinal granulomas (Fig. 6 E, G, Suppl. Fig. 5 A). This contrasts
309 with the naïve condition in which macrophages and neutrophils are distributed across
310 the intestine (Supp. Fig. 5 B,C).

311 While many of the cell types found to be co-localized around and within granuloma
312 niches (macrophages, neutrophils, dendritic cells and $CD4^+$ T cells) have been shown to
313 be associated with helminth-induced granulomas, the involvement of mast cells, pDCs
314 and Lymphoid Tissue inducer (LTi) cells has yet to be reported. Eosinophils are among
315 the immune cell types associated with granulomas but as they are not represented in
316 the scSeq datasets (due to high endogenous RNase expression) we were not able to
317 distinguish them as an individual category. The presence of pDCs within the granuloma
318 is unexpected, given their classical role as a mediator of anti-viral immune responses,
319 but reflects highest expression of pDC markers *Siglech*, *Klk1* and *Cox6a2* [74, 75] in the
320 annotated cluster (Supp. Fig. 5 D). The role of pDCs as a granuloma-associated cell type
321 during helminth infection thus needs to be investigated.

322 *2.7 Cell-to-cell interactions and signalling pathways.*

323 Following characterisation of cell types and gene expression within each spatially
324 resolved niche in the infected murine gut, we turned to the question of interactions and
325 molecular dialogue between these niches, by identifying complementary ligand-
326 receptor pairings using CellChatp [76]. From the granuloma niche, all predicted
327 interactions were with the lower crypt, and indeed these represented the highest
328 number of predicted interactions in the whole study (Fig. 7 A). Numerous interactions

329 were also noted between other sites, connecting the lower crypt in particular with the
330 upper crypt and villi that were not predicted to directly interact with granuloma
331 products.

332 Enriched predicted signalling between the granuloma and lower crypt niches primarily
333 represented immune cell activation and differentiation pathways. Dominant
334 chemokines in the granuloma profile are CCL6, CCL7, CCL8 and CCL12, with the
335 CCL8/CCR5 pairing with the lower crypt acting in a bidirectional manner, likely to
336 underpin the activated myeloid and lymphoid populations recruited to the granuloma,
337 while also able to act on chemokine receptors in the lower crypt (Fig. 7 B, C).
338 Interestingly, the among the strongest interactions is between the chemokine-like
339 macrophage migration inhibitory factor (MIF) expressed in both the lower crypt and the
340 granuloma, and its receptors CD74 and CD44 present in both niches (Fig. 7 B, C), as this
341 chemokine-like mediator is known to be essential for immunity to *H. polygyrus* as well
342 as to the rat nematode *Nippostrongylus brasiliensis* [77].

343 As may be expected for the tissue remodelling involved in granuloma formation, there
344 are prominent interactions with ligands for extracellular matrix and proteoglycan
345 including pleiotrophin (*Ptn*) which binds heparin and the syndecin receptors *Sdc1, Sdc3*
346 and *Sdc4* as well as nucleolin (*Ncl*), and the IL-6-like cytokine Oncostatin M (*Osm*) (Fig.
347 7 C). Particularly conspicuous is *Spp1* (secreted phosphoprotein 1, also known as
348 sialoprotein or osteopontin) which binds CD44 and integrins such as α4 [78], and in a
349 comparative pathway analysis of the 3 tissues sites, is found to be prominent in
350 granulomas (Fig. 7 D). Spp1 can also interact with αv integrins involved in activation of
351 latent TGF-β. Indeed, TGF-β signalling adopts a high profile in both granuloma-crypt
352 interactions, primarily represented by TGF-β1 from the granuloma binding the
353 canonical TGF-β receptors, but also signals from the lower crypt to the upper crypt (Fig.
354 7 B, C). It is known that blocking TGF-β signalling promotes expulsion of *H. polygyrus* [79],
355 and most intriguingly that this parasite secretes mimics of TGF-β that bind the same
356 receptors together with CD44 [28, 80]. Combined mapping of key ligand-receptor pairs
357 reveals their spatial restriction , largely to the sites of granulomas, although MIF-CD74-
358 CD44 appears to be more generalised through the infected tissue (Fig. 7 E).

359 Collectively, these findings demonstrate a progressive disruption of epithelial renewal
360 and immune-epithelial crosstalk during *H. polygyrus* infection. Early suppression of Wnt
361 signalling (day 3) precedes Notch-dominated differentiation (day 7), a pattern that has
362 been previously linked to helminth-induced epithelial remodelling. Concurrently, crypt-
363 granuloma interactions evolve from inflammatory (IL-6-driven, day 5) to a tissue
364 remodelling state (TGF-β, osteopontin, day 7), reflecting the dual nature of the host
365 response - attempting both parasite clearance and damage repair. These results
366 reinforce the notion that *H. polygyrus* actively reshapes its host environment,
367 leveraging immune suppression and epithelial reprogramming to establish chronic
368 infection. Understanding these spatially distinct and time-dependent interactions
369 provides deeper insight into how helminths exploit the gut niche and highlight potential
370 targets for therapeutic intervention.

371 **3. Discussion**

372 Spatial transcriptomics has emerged as a powerful tool to unravel the intricacies of gene
373 expression patterns within the complex architecture of tissues [81]. In this study, we
374 employed the Visium platform to conduct spatial transcriptomics on murine small
375 intestine tissues, providing a comprehensive view of the transcriptional landscape
376 during steady-state conditions and in response to *H. polygyrus* infection. Furthermore,
377 we uncover the localisation of various cell types within the context of steady state and
378 helminth-infected intestines and infer the cell-cell interactions that take place between
379 them.

380 Upon *H. polygyrus* infection, dynamic transcriptional changes were observed in the
381 small intestine, particularly within the granuloma and surrounding areas. One such
382 change is the apparent upregulation of tight junction genes in the helminth infected gut
383 compared to the naive, which could impair the host's ability to increase fluid egress as
384 part of the 'weep and sweep' response against helminths. In addition, as *H. polygyrus*
385 infection can lead to the suppression of differentiated specialist epithelial cells like
386 goblet, Paneth and tuft cells [15, 18, 32], this may explain attenuated expression of specific
387 stem cell differentiation genes of the crypt areas.

388 The transcriptomic analysis at day 7 post-infection revealed a multifaceted immune
389 response, with distinct granuloma signatures categorized into clusters based on the
390 distance to the parasite, which may be indicative of a longitudinal response to the
391 parasite from active inflammation to resolution of the immune response. While the
392 parasite is still present within the granuloma, a variety of type 2 immune response
393 factors are expressed, including *Fcer1g* and products of M2 phenotype macrophages
394 like *Arg1* and *Retlna*, all of which are associated with the clearance/expulsion of
395 parasites. Once the parasite is no longer detected in the granuloma, there is a return
396 towards homeostasis, with an increase in extracellular matrix remodelling and
397 maintenance of the intestinal barrier through keratin deposition.

398 Despite potential limitations of deconvolution approaches, they allowed us to leverage
399 spatially resolved neighbourhoods with existing single cell data to predict cell-to-cell
400 interactions of spatial niches within the small intestine. Common signatures of cell type
401 colocalization were identified, particularly in the crypts and villi, emphasizing the
402 coordinated organization of various cell types within specific tissue regions. Specific
403 colocalization patterns in *H. polygyrus* infection, particularly in the granulomas,
404 highlighted the cellular interactions occurring during the host response to parasitic
405 infection. In contrast, in the steady-state there is negligible activity from immune cells
406 and the interactome is rather associated with epithelial cell differentiation and
407 maintaining tissue integrity of the intestine. Thus, this landscape is dramatically altered
408 in response to parasitic infection and the formation of granulomas.

409 Although our study demonstrates the heterogeneity of the host response across
410 different spatial compartments of the intestine during *H. polygyrus* infection, the
411 advent of higher-resolution spatial sequencing techniques would allow insight into the
412 transcriptomic landscape of individual cells, and potentially the helminth itself, within
413 their native spatial context. This will offer insights into cell types, their spatial
414 distribution, potential heterogeneity within specific regions, and interactions with the
415 parasite, enabling a comprehensive characterization of the dynamic host-pathogen
416 interplay. Future work includes integrating additional time points of *H. polygyrus*
417 infection in the murine intestine to map the spatial-temporal dynamics of the interplay
418 of the host immune system and gut epithelia. These insights gained from our study lay

419 the groundwork for future investigations into the molecular mechanisms driving host
420 defence and tissue responses during parasitic infections. To conclude, this report
421 highlights the main strengths of spatial transcriptomics, which is to access and unravel
422 previously inaccessible details, paving the way for a more in-depth comprehension of
423 the molecular and spatial dimensions of host immune responses and tissue-specific
424 adaptations to parasitic challenges.

425 **4. Materials and Methods**

426 *4.1 Mice and parasites*

427 Eight-week-old female C57BL/6 mice purchased from Envigo UK and housed in
428 individually ventilated cages were used throughout this study. All animal studies were
429 performed under the UK Home Office Licence and approved by the University of
430 Glasgow Animal Welfare and Ethical Review Board. Mice were infected by oral gavage
431 with 400 infective third-stage larvae (L3) *H. polygyrus*, maintained as previously
432 described [82]. Mice were culled on days 3, 5 and 7 post-infection.

433 *4.2 Immunohistochemistry*

434 Gut roll sections were made using a microtome through the gut rolls at a thickness of 5
435 µm before mounting on glass slides. Sections were deparaffinized by immersing slides
436 in xylene, then hydrated through 100%, 90%, and 70% ethanol successively. Heat-
437 induced epitope retrieval was performed in citrate buffer (Thermo Fisher Scientific), and
438 then sections were blocked using 2.5% normal horse serum blocking solution (Vector
439 Laboratories) for 1 h at room temperature. Slides were then incubated overnight at 4°C
440 with the corresponding Ab () in 2.5% normal horse serum blocking solution. Polyclonal
441 rabbit IgGs (Abcam) were used as an isotype control. After washing, sections were
442 incubated with specific AlexaFluor secondary Abs (1:1000), washed, stained with DAPI
443 for 5 min and finally mounted using Heatshields Vectashield HardSet Antifade Mounting
444 Medium (Vector Laboratories). Slides were imaged using a Nikon-AX inverted
445 microscope. The resulting image files were analysed using ImageJ/Fiji.

446 *4.3 Tissue processing and library preparation*

447 Processing small intestine tissue involved the removal of the gut-associated adipose
448 tissue following which luminal contents were removed by washing with cold PBS.
449 Starting from the most distal end, the small intestine was mounted onto a wooden
450 skewer with the luminal side facing outwards. After 4 h fixing in 4% NBF, tissue was cut
451 longitudinally and rolled creating a gut roll with the distal small intestine at the centre.
452 The roll was then left to fix overnight, followed by processing and embedding in paraffin
453 [83]. Five µm sections, which included at least one granuloma, were made using a

454 microtome and placed on Visium 10x Genomics slides (PN-2000233), fitting the four
455 6.5mm² capture areas (Fig. 1).

456 For analysis, slides with small intestine tissue were stained with H&E, and imaged by
457 NanoZoomer-SQ Digital slide scanner. Sequence libraries were processed per the
458 manufacturer's instructions (10x Genomics, Visium Spatial Transcriptomic). After cDNA
459 strand synthesis, cDNA was quantified using quantitative RT-PCR ABI 7500 Fast Real-
460 Time PCR System and analysed with ABI 7500 Software 2.3 (Fig. 1).

461 *4.4 Sequencing and data processing*

462 Visium libraries were sequenced using a P3 flow cell to a minimum of 200 million reads
463 per sample on the NextSeq2000 instrument, paired-end 2x100bp. The sample images
464 were then analysed and spots were assigned a metadata value according to the type of
465 tissue the spot captured: Crypt, Villus, Peyer's Patch and in infected tissues also
466 Granuloma and *H. polygyrus* (referred to as 'Worm'). Samples were mapped against the
467 *Mus musculus* mm10 reference using 10X Genomics' Spaceranger version 2.1.1 (10X
468 Genomics) on default parameters except for the loupe alignment JSON file, which was
469 edited so that unlabelled spots were also included in the final mapping output. The
470 Spaceranger mapped Naive, D3, D5 and D7 samples underwent quality control using
471 SCANPY [84], with spots with high UMI counts detected across the samples removed.

472 *4.5 Comparison of crypts and villi across* H. polygyrus *infection*

473 The quality controlled naïve, D3, D5 and D7 samples were concatenated together into
474 an AnnData object, with only the genes that were detected in all four of the datasets
475 being present in the concatenated dataset. The expression values were normalised by
476 their total sum, and each cells normalised counts scaled to the median UMI count of the
477 concatenated object. These values were then log1p transformed.

478 A series of differential expressed gene analyses were carried out across the infection
479 time series. The concatenated object was split into two objects for spots labelled 'Crypt'
480 or 'Villi'. For these datasets, each timepoint of interest was compared to its adjacent
481 time points. For example, the D5 sample was compared against the D3 and D7 samples,

482 while the naive sample was compared against the D3 sample. Differentially expressed
483 genes were defined as those with a Benjamini-Hochberg corrected p-value < 0.05, with
484 p-values generated using a Mann Whitney U test as the default method of SCANPY.

485 *4.6 Characterising granulomas within* H. polygyrus-*infected mice intestine*

486 The mapped and quality controlled D5 and D7 post *H. polygyrus* infection samples were
487 loaded into SCANPY [84], concatenated into a single AnnData object, and the spots
488 designated as 'Granuloma' were extracted. Expression values of the spots were
489 normalized by their total UMI counts and scaled so they added up to the median total
490 UMI counts of the concatenated object. These values were then log1p transformed. The
491 top 2000 variable genes were found using default parameters from SCANPY. Principal
492 Components analysis was carried out on the normalized expression data using only the
493 genes identified as being highly variable, and batch correction of the PCA space was
494 carried out using Harmony. A nearest neighbours (nn) graph was constructed using the
495 first 10 Harmony-adjusted PCs, with this graph being used as the basis for Leiden
496 clustering (resolution = 0.4) and UMAP [85]. Marker genes of the resulting Leiden clusters
497 were identified using SCANPY's rank_genes_groups function, using t-test to assess for
498 statistical significance and Benjamini-Hochberg to adjust the p-value to correct for
499 multiple-testing.

500 *4.7 Loupe browser*

501 Loupe Browser (v.5.0.0; 10X Genomics) is a desktop application compatible with
502 Windows and Macintosh operating systems. It facilitates the easy visualisation and
503 analysis of Visium gene expression data. This software is employed for the identification
504 of significant genes and cell types, as well as for exploring substructures within cell
505 clusters. The Loupe Browser viewer utilises single points representing cell barcodes. To
506 visualise data within the Loupe Browser 2D space, Cell Ranger transfers Principal
507 Components Analysis (PCA)-reduced data into a t-SNE (t-Stochastic Neighbour
508 Embedding) plot. T-SNE is a nonlinear dimensionality reduction method with
509 modifications by 10X Genomics. Loupe Browser includes a "Categories" mode, allowing
510 users to label subpopulations of cells in the clustering plot with specific categories.

511 *4.8 Preparing the single-cell RNA sequencing reference datasets*

512 The raw expression matrices and metadata of the Xu *et al*. [72] and Haber *et al.* [73] scRNA-
513 seq data were loaded into Seurat [86]. For the Xu data, more quality control of the samples
514 was carried out. This consisted of removing cells with remarkably high/low
515 nFeature_counts and also those with a high percentage of mitochondrial reads per cell.
516 The cut-off values can be seen by viewing the relevant code on our GitHub. The
517 metadata of the Xu set were then simplified, with the cell types being designated as
518 'low UMI' being merged with their regular UMI counterparts and specific subsets of cell
519 type e.g. 'DC (Cd103+ Cd11b+)', 'DC (Cd103+ Cd11b-)' and 'DC (Cd103- C2)' being
520 simplified as just 'DC'. Nonimmune cells were also removed from the Xu datasets. The
521 Xu and Haber Seurat objects were then merged and converted into h5ad format.

522 *4.9 Cell2location analysis of* H. polygyrus *infected and naïve mice intestine*

523 For setting up the model of the Xu and Haber merged scRNA-seq dataset, we used the
524 sequencing run of each of the datasets as the 'batch_key' and included the condition of
525 the datasets (e.g. allergy, parasite infected, naive/control) as a categorical covariate.
526 The training parameters for the training of the Visium slide model in cell2location [86]
527 were chosen as follows. Within all the D3, D5, D7 and naïve Visium samples there was
528 variation in total UMI counts that could not be explained by the tissue, thus the RNA
529 detection sensitivity parameter was set to 20, as per the recommendation of the
530 cell2location authors. The number of cells per location was chosen to be 50, based on
531 visual observation of the scanned slides. The models were trained on a GPU with 80 Gb
532 of RAM. The 5% quantile cell abundance was stored in the Visium anndata objects and
533 used for all subsequent analysis and visualisation.

534 Non-negative factorization (NMF) analysis in cell2location was carried out, using the
535 concatenation of the new length and depth coordinates and the original Visium
536 coordinates as the spatial basis for the NMF. For the D7 sample, 7 factors were created,
537 five factors were created for the D5 sample, while three factors were created for the
538 naïve and D3 samples.

539 *4.10 Cellular communication inference of* H. polygyrus *infection in the murine intestine*

540 Spatial niches defined by the NMF factorisation analysis yielded three distinct spatially
541 resolved neighbourhoods termed the villi, upper crypt, lower crypt and granuloma
542 niche. Spots assigned these labels were fed into CellChat (v.2.1.1) [76] alongside the
543 spatial coordinates from the full resolution tissue image to allow resulting interactions
544 to be within spatial constraints. The conversion of spatial coordinates from pixels to
545 micrometres was calculated using the ratio of the theoretical spot size set to 55um over
546 the number of pixels that cover the diameter of the spot. In addition to this, the
547 communication probability of two cells interacting was also restricted with a contact
548 range set to 100 as recommended by the CellChat 10X Visium workflow. The CellChat
549 database used was set to the organism '*mouse*' and all functional interaction
550 annotations were used except those classified as '*Non-protein Signalling*' to avoid the
551 inclusion of interactions involving synaptic signalling which lies outside the context of
552 the murine intestinal tissue.

553 *4.11 Package versions*

554 Python version 3.10.12 was used with the following packages: Pandas – v.1.5.3, Numpy
555 – v.1.23.0, SCANPY – v.1.9.3 [76], anndata – v.0.8.0, squidpy – v.1.3.1, scipy – v.1.10.1,
556 sklearn – v.1.3.0, cell2location – v.0.1.3. R version v.4.2.2 was used with the following
557 packages: Seurat – v.4.3.0, harmony – v.1.2.0, SeuratDisk – v.0.0.0.9020, CellChat –
558 v.2.1.1. When training the cell2location models on GPUs, Python v.3.10.9 was used
559 along with the following package versions: cell2location – v.0.1.4, scipy – v.1.10.0,
560 SCANPY – v.1.9.6, scikit-learn – v.1.2.1, numpy – v.1.23.4, pandas – v.2.1.4.

561 *4.12 Code availability*

562 The code to replicate this analysis can be found at the following github repository:
563 https://github.com/No2Ross/Visium_Hpolygyrus_gut

564 **Acknowledgements**

565 We thank Dr Juan Quintana for expert advice and Claire Ciancia for excellent technical
566 assistance. The authors gratefully acknowledge Glasgow Polyomics (University of
567 Glasgow) for their support and assistance.

568 **Funding**

569 M.C.P. and R.M.M were supported by the Wellcome Trust through an Investigator
570 Award to RMM (Ref 219530), and the Wellcome Trust core-funded Wellcome Centre
571 for Integrative Parasitology (Ref: 104111), including an Early Career Researchers
572 Futurescope grant from the Centre. R.F.L was funded by the Medical Research Council
573 through their Precision Medicine DTP (MRC grant number: MR/N013166/1). O.H was
574 funded by the Research into Inflammatory Arthritis Centre Versus Arthritis UK, based in
575 the Universities of Glasgow, Birmingham, Newcastle and Oxford.

576 **Author contributions**

577 All authors helped shape the research, analysis, and manuscript. The study was
578 designed by M.C.P. and R.M.M. with input from T.O. M.C.P., O.H and R.F.L generated
579 the data, performed the analysis and drafted the manuscript figures and text. R.M.M
580 and T.O. provided critical feedback and edited the manuscript prior to submission.

581 **Declaration of interest**

582 The authors declare no competing interests

583 **References**

584 1. Hotez, P.J. *et al.* Helminth infections: the great neglected tropical diseases. *J Clin Invest*
585 **118**, 1311-1321 (2008).
586 2. Charlier, J. *et al.* Initial assessment of the economic burden of major parasitic helminth
587 infections to the ruminant livestock industry in Europe. *Prev Vet Med* **182**, 105103
588 (2020).
589 3. Monroy, F.G. & Enriquez, F.J. *Heligmosomoides polygyrus :* a model for chronic
590 gastrointestinal helminthiasis. *Parasitol Today* **8**, 49-54 (1992).
591 4. Reynolds, L.A., Filbey, K.J. & Maizels, R.M. Immunity to the model intestinal helminth
592 parasite *Heligmosomoides polygyrus*. *Semin Immunopathol* **34**, 829-846 (2012).
593 5. Anthony, R.M. *et al.* Memory T_H2 cells induce alternatively activated macrophages to
594 mediate protection against nematode parasites. *Nat Med* **12**, 955-960 (2006).
595 6. Filbey, K.J. *et al.* Innate and adaptive type 2 immune cell responses in genetically
596 controlled resistance to intestinal helminth infection. *Immunol Cell Biol* **92**, 436-448
597 (2014).
598 7. Lechner, A., Bohnacker, S. & Esser-von Bieren, J. Macrophage regulation & function in
599 helminth infection. *Semin Immunol* **53**, 101526 (2021).
600 8. Harris, N.L. & Loke, P. Recent advances in Type-2-cell-mediated immunity: insights
601 from helminth infection. *Immunity* **47**, 1024-1036 (2017).
602 9. Chen, F. *et al.* Helminth resistance is mediated by differential activation of recruited
603 monocyte-derived alveolar macrophages and arginine depletion. *Cell Rep* **38**, 110215
604 (2022).
605 10. Maizels, R.M. & Gause, W.C. Targeting helminths: The expanding world of type 2
606 immune effector mechanisms. *J Exp Med* **220:** e20221381 (2023).
607 11. Wahid, F.N., Behnke, J.M., Grencis, R.K., Else, K.J. & Ben-Smith, A.W. Immunological
608 relationships during primary infection with *Heligmosomoides polygyrus :* Th2
609 cytokines and primary response phenotype. *Parasitology* **108**, 461-471 (1994).
610 12. Finney, C.A.M., Taylor, M.D., Wilson, M.S. & Maizels, R.M. Expansion and activation of
611 $CD4^+CD25^+$ regulatory T cells in *Heligmosomoides polygyrus* infection. *European*
612 *Journal of Immunology* **37**, 1874-1886 (2007).

613 13. Rausch, S. *et al.* Functional analysis of effector and regulatory T cells in a parasitic
614 nematode infection. *Infect Immun***76**, 1908-1919 (2008).
615 14. Smith, K.A. *et al.* Low level regulatory T cell activity is essential for functional type-2
616 effector immunity to expel gastrointestinal helminths. . *Mucosal Immunol* **9**, 428-443
617 (2016).
618 15. Nusse, Y.M. *et al.* Parasitic helminths induce fetal-like reversion in the intestinal stem
619 cell niche. *Nature* **559**, 109-113 (2018).
620 16. Progatzky, F. *et al.* Regulation of intestinal immunity and tissue repair by enteric glia.
621 *Nature* **599**, 125-130 (2021).
622 17. Ariyaratne, A. & Finney, C.A.M. Eosinophils and macrophages within the Th2-induced
623 granuloma: balancing killing and healing in a tight space. *Infect Immun* **87**, e00127-19
624 (2019).
625 18. Drurey, C. *et al.* Intestinal epithelial tuft cell induction is negated by a murine helminth
626 and its secreted products. *J Exp Med* **219**: e20211140 (2022).
627 19. Peterson, L.W. & Artis, D. Intestinal epithelial cells: regulators of barrier function and
628 immune homeostasis. *Nat Rev Immunol* **14**, 141-153 (2014).
629 20. Gieseck, R.L., 3rd, Wilson, M.S. & Wynn, T.A. Type 2 immunity in tissue repair and
630 fibrosis. *Nat Rev Immunol* **18**, 62-76 (2018).
631 21. Inclan-Rico, J.M., Rossi, H.L. & Herbert, D.R. Every cell is an immune cell; contributions
632 of non-hematopoietic cells to anti-helminth immunity. *Mucosal Immunol* **15**: 1199-
633 1211 (2022).
634 22. Hewitson, J.P. *et al.* Concerted activity of IgG1 antibodies and IL-4/IL-25-dependent
635 effector cells trap helminth larvae in the tissues following vaccination with defined
636 secreted antigens, providing sterile immunity to challenge infection. *PLoS Pathog* **11**,
637 e1004676 (2015).
638 23. Matsuda, R. *et al.* A TNF-IL-1 circuit controls Yersinia within intestinal pyogranulomas.
639 *J Exp Med* **221** (2024).
640 24. Reynolds, L.A. *et al.* MyD88 signaling inhibits protective immunity to the
641 gastrointestinal helminth parasite *Heligmosomoides polygyrus*. *Journal of*
642 *immunology* **193**, 2984-2993 (2014).
643 25. Shimokawa, C. *et al.* Mast cells are crucial for induction of group 2 innate lymphoid
644 cells and clearance of helminth infections. *Immunity* **46**, 863-874 e864 (2017).

645 26. Pelly, V.S. *et al.* IL-4-producing ILC2s are required for the differentiation of TH2 cells
646 following *Heligmosomoides polygyrus* infection. *Mucosal Immunol* **9**, 1407-1417
647 (2016).
648 27. Ahrends, T. *et al.* Enteric pathogens induce tissue tolerance and prevent neuronal loss
649 from subsequent infections. *Cell* **184**, 5715-5727 e5712 (2021).
650 28. Johnston, C.J.C. *et al.* A structurally distinct TGF-β mimic from an intestinal helminth
651 parasite potently induces regulatory T cells. . *Nature Communications* **8**, 1741 (2017).
652 29. Maizels, R.M., McSorley, H.J., Smits, H.H., ten Dijke, P. & Hinck, A.P. Cytokines from
653 parasites: Manipulating host responses by molecular mimicry. *Biochem J* **482**, 443-339
654 (2025).
655 30. Rubtsov, Y.P. & Rudensky, A.Y. TGFβ signalling in control of T-cell-mediated self-
656 reactivity. *Nat Rev Immunol* **7**, 443-453 (2007).
657 31. Sanjabi, S., Oh, S.A. & Li, M.O. Regulation of the immune response by TGF-β: from
658 conception to autoimmunity and infection. *Cold Spring Harb Perspect Biol* **9**, a022236
659 (2017).
660 32. Karo-Atar, D. *et al.* Helminth-induced reprogramming of the stem cell compartment
661 inhibits type 2 immunity. *J Exp Med* **219,** e20212311 (2022).
662 33. Williams, C.G., Lee, H.J., Asatsuma, T., Vento-Tormo, R. & Haque, A. An introduction
663 to spatial transcriptomics for biomedical research. *Genome Med* **14**, 68 (2022).
664 34. Parigi, S.M. *et al.* The spatial transcriptomic landscape of the healing mouse intestine
665 following damage. *Nat Commun* **13**, 828 (2022).
666 35. Wood, C.S. *et al.* Spatially resolved transcriptomics deconvolutes prognostic
667 histological subgroups in patients with colorectal cancer and synchronous liver
668 metastases. *Cancer Res* **83**, 1329-1344 (2023).
669 36. Jang, B.G. *et al.* SMOC2, an intestinal stem cell marker, is an independent prognostic
670 marker associated with better survival in colorectal cancers. *Sci Rep* **10**, 14591 (2020).
671 37. Cheng, Z.F. & Cartwright, C.A. Rack1 maintains intestinal homeostasis by protecting
672 the integrity of the epithelial barrier. *Am J Physiol Gastrointest Liver Physiol* **314**, G263-
673 G274 (2018).
674 38. Friederich, E., Pringault, E., Arpin, M. & Louvard, D. From the structure to the function
675 of villin, an actin-binding protein of the brush border. *Bioessays* **12**, 403-408 (1990).

676 39. Wosen, J.E., Mukhopadhyay, D., Macaubas, C. & Mellins, E.D. Epithelial MHC Class II
677 expression and its role in antigen presentation in the gastrointestinal and respiratory
678 tracts. *Front Immunol* **9**, 2144 (2018).
679 40. Wynn, T.A. Fibrotic disease and the T(H)1/T(H)2 paradigm. *Nat Rev Immunol* **4**, 583-
680 594 (2004).
681 41. Perochon, J., Carroll, L.R. & Cordero, J.B. Wnt signalling in intestinal stem cells: lessons
682 from mice and flies. *Genes (Basel)* **9**, 9030138 (2018).
683 42. Barker, N. *et al.* Identification of stem cells in small intestine and colon by marker gene
684 Lgr5. *Nature* **449**, 1003-1007 (2007).
685 43. Ehrencrona, E. *et al.* The IgGFc-binding protein FCGBP is secreted with all GDPH
686 sequences cleaved but maintained by interfragment disulfide bonds. *J Biol Chem* **297**,
687 100871 (2021).
688 44. Nonnecke, E.B. *et al.* Characterization of an intelectin-1 (Itln1) knockout mouse model.
689 *Front Immunol* **13**, 894649 (2022).
690 45. Bergstrom, J.H. *et al.* Gram-positive bacteria are held at a distance in the colon mucus
691 by the lectin-like protein ZG16. *Proc Natl Acad Sci U S A* **113**, 13833-13838 (2016).
692 46. Chen, G. *et al.* EpCAM is essential for maintenance of the small intestinal epithelium
693 architecture via regulation of the expression and localization of proteins that compose
694 adherens junctions. *Int J Mol Med* **47**, 621-632 (2021).
695 47. Baumholtz, A.I., Gupta, I.R. & Ryan, A.K. Claudins in morphogenesis: Forming an
696 epithelial tube. *Tissue Barriers* **5**, e1361899 (2017).
697 48. Panarelli, N.C., Yantiss, R.K., Yeh, M.M., Liu, Y. & Chen, Y.T. Tissue-specific cadherin
698 CDH17 is a useful marker of gastrointestinal adenocarcinomas with higher sensitivity
699 than CDX2. *Am J Clin Pathol* **138**, 211-222 (2012).
700 49. Entwistle, L.J. *et al.* Epithelial-cell-derived phospholipase A2 group 1b is an
701 endogenous anthelmintic. *Cell Host Microbe* **22**, 484-493 e485 (2017).
702 50. Xi, R. *et al.* Up-regulation of gasdermin C in mouse small intestine is associated with
703 lytic cell death in enterocytes in worm-induced type 2 immunity. *Proc Natl Acad Sci U*
704 *S A* **118** (2021).
705 51. Liao, Y., Xiao, N., Wang, X., Dai, S. & Wang, G. Promoting effect of Tmsb4x on the
706 differentiation of peripheral blood mononuclear cells to dendritic cells during
707 septicemia. *Int Immunopharmacol* **111**, 109002 (2022).

708 52. Mahley, R.W. Apolipoprotein E: cholesterol transport protein with expanding role in
709 cell biology. *Science* **240**, 622-630 (1988).
710 53. Lee, M.Y. & Griendling, K.K. Redox signaling, vascular function, and hypertension.
711 *Antioxid Redox Signal* **10**, 1045-1059 (2008).
712 54. Wang, Y. *et al.* A novel role for villin in intestinal epithelial cell survival and
713 homeostasis. *J Biol Chem* **283**, 9454-9464 (2008).
714 55. Wood, M.B., Rios, D. & Williams, I.R. TNF-alpha augments RANKL-dependent intestinal
715 M cell differentiation in enteroid cultures. *Am J Physiol Cell Physiol* **311**, C498-507
716 (2016).
717 56. Turner, H. & Kinet, J.P. Signalling through the high-affinity IgE receptor Fc epsilonRI.
718 *Nature* **402**, B24-30 (1999).
719 57. Jablonski, K.A. *et al.* Novel Markers to Delineate Murine M1 and M2 Macrophages.
720 *PLoS One* **10**, e0145342 (2015).
721 58. Capuano, A. *et al.* Integrin binding site within the gC1q domain orchestrates EMILIN-
722 1-induced lymphangiogenesis. *Matrix Biol* **81**, 34-49 (2019).
723 59. Kashiba, M., Terashima, M., Sagawa, T., Yoshimura, S. & Yamamoto, Y. Prosaposin
724 knockdown in Caco-2 cells decreases cellular levels of coenzyme Q10 and ATP, and
725 results in the loss of tight junction barriers. *J Clin Biochem Nutr* **60**, 81-85 (2017).
726 60. Pendse, M. *et al.* Macrophages regulate gastrointestinal motility through complement
727 component 1q. *Elife* **12**, e78558 (2023).
728 61. Bergstrom, J.H. *et al.* AGR2, an endoplasmic reticulum protein, is secreted into the
729 gastrointestinal mucus. *PLoS One* **9**, e104186 (2014).
730 62. Qu, M. *et al.* Establishment of intestinal organoid cultures modeling injury-associated
731 epithelial regeneration. *Cell Res* **31**, 259-271 (2021).
732 63. Shen, Y. *et al.* Matrix remodeling associated 7 proteins promote cutaneous wound
733 healing through vimentin in coordinating fibroblast functions. *Inflamm Regen* **43**, 5
734 (2023).
735 64. Martire, S. & Banaszynski, L.A. The roles of histone variants in fine-tuning chromatin
736 organization and function. *Nat Rev Mol Cell Biol* **21**, 522-541 (2020).
737 65. Dever, T.E., Dinman, J.D. & Green, R. Translation elongation and recoding in
738 eukaryotes. *Cold Spring Harb Perspect Biol* **10**: a032649 (2018).

739 66. Ghanem, L.R. *et al.* Poly(C)-binding protein Pcbp2 enables differentiation of definitive
740 erythropoiesis by directing functional splicing of the Runx1 transcript. *Mol Cell Biol* **38**
741 e00175-18. (2018).
742 67. Soni, K. *et al.* Structural basis for specific RNA recognition by the alternative splicing
743 factor RBM5. *Nat Commun* **14**, 4233 (2023).
744 68. Delom, F., Mohtar, M.A., Hupp, T. & Fessart, D. The anterior gradient-2 interactome.
745 *Am J Physiol Cell Physiol* **318**, C40-C47 (2020).
746 69. Pin, G. *et al.* Down-regulation of PDCD4 promotes proliferation, angiogenesis and
747 tumorigenesis in glioma cells. *Front Cell Dev Biol* **8**, 593685 (2020).
748 70. Newman, A.M. *et al.* Determining cell type abundance and expression from bulk
749 tissues with digital cytometry. *Nat Biotechnol* **37**, 773-782 (2019).
750 71. Kleshchevnikov, V. *et al.* Cell2location maps fine-grained cell types in spatial
751 transcriptomics. *Nat Biotechnol* **40**, 661-671 (2022).
752 72. Xu, H. *et al.* Transcriptional atlas of intestinal immune cells reveals that neuropeptide
753 α-CGRP orchestrates ILC2 responses. *Immunity* **51**: 696-708 (2019).
754 73. Haber, A.L. *et al.* A single-cell survey of the small intestinal epithelium. *Nature* **551**,
755 333-339 (2017).
756 74. Blasius, A.L. & Colonna, M. Sampling and signaling in plasmacytoid dendritic cells: the
757 potential roles of Siglec-H. *Trends Immunol* **27**, 255-260 (2006).
758 75. Valente, M. *et al.* Novel mouse models based on intersectional genetics to identify and
759 characterize plasmacytoid dendritic cells. *Nat Immunol* **24**, 714-728 (2023).
760 76. Jin, S. *et al.* Inference and analysis of cell-cell communication using CellChat. *Nat*
761 *Commun* **12**, 1088 (2021).
762 77. Filbey, K.J. *et al.* Macrophage migration inhibitory factor (MIF) is essential for type 2
763 effector cell immunity to an intestinal helminth parasite. *Frontiers in Immunology* **10**,
764 2375 (2019).
765 78. Hui, T., Sorensen, E.S. & Rittling, S.R. Osteopontin binding to the alpha 4 integrin
766 requires highest affinity integrin conformation, but is independent of post-
767 translational modifications of osteopontin. *Matrix Biol* **41**, 19-25 (2015).
768 79. Grainger, J.R. *et al.* Helminth secretions induce *de novo* T cell Foxp3 expression and
769 regulatory function through the TGF-β pathway. *J Exp Med* **207**, 2331-2341 (2010).

770 80. van Dinther, M. *et al.* CD44 acts as a co-receptor for cell-specific enhancement of
771 signaling and regulatory T cell induction by TGM1, a parasite TGF-β mimic. *Proc Natl*
772 *Acad Sci U S A* **120**, e2302370120 (2023).
773 81. Joulia, R. *et al.* A single-cell spatial chart of the airway wall reveals proinflammatory
774 cellular ecosystems and their interactions in health and asthma. *Nat Immunol* **26**, 920-
775 933 (2025).
776 82. Johnston, C.J. *et al.* Cultivation of *Heligmosomoides polygyrus*: an immunomodulatory
777 nematode parasite and its secreted products. *J Vis Exp*, **98:** e52412 (2015).
778 83. Bialkowska, A.B., Ghaleb, A.M., Nandan, M.O. & Yang, V.W. Improved Swiss-rolling
779 technique for intestinal tissue preparation for immunohistochemical and
780 immunofluorescent analyses. *J Vis Exp* (2016) 113:54161.
781 84. Wolf, F.A., Angerer, P. & Theis, F.J. SCANPY: large-scale single-cell gene expression
782 data analysis. *Genome Biol* **19**, 15 (2018).
783 85. Traag, V.A., Waltman, L. & van Eck, N.J. From Louvain to Leiden: guaranteeing well-
784 connected communities. *Sci Rep* **9**, 5233 (2019).
785 86. Hao, Y. *et al.* Dictionary learning for integrative, multimodal and scalable single-cell
786 analysis. *Nat Biotechnol* **42**, 293-304 (2024).
787 .

Figure 1

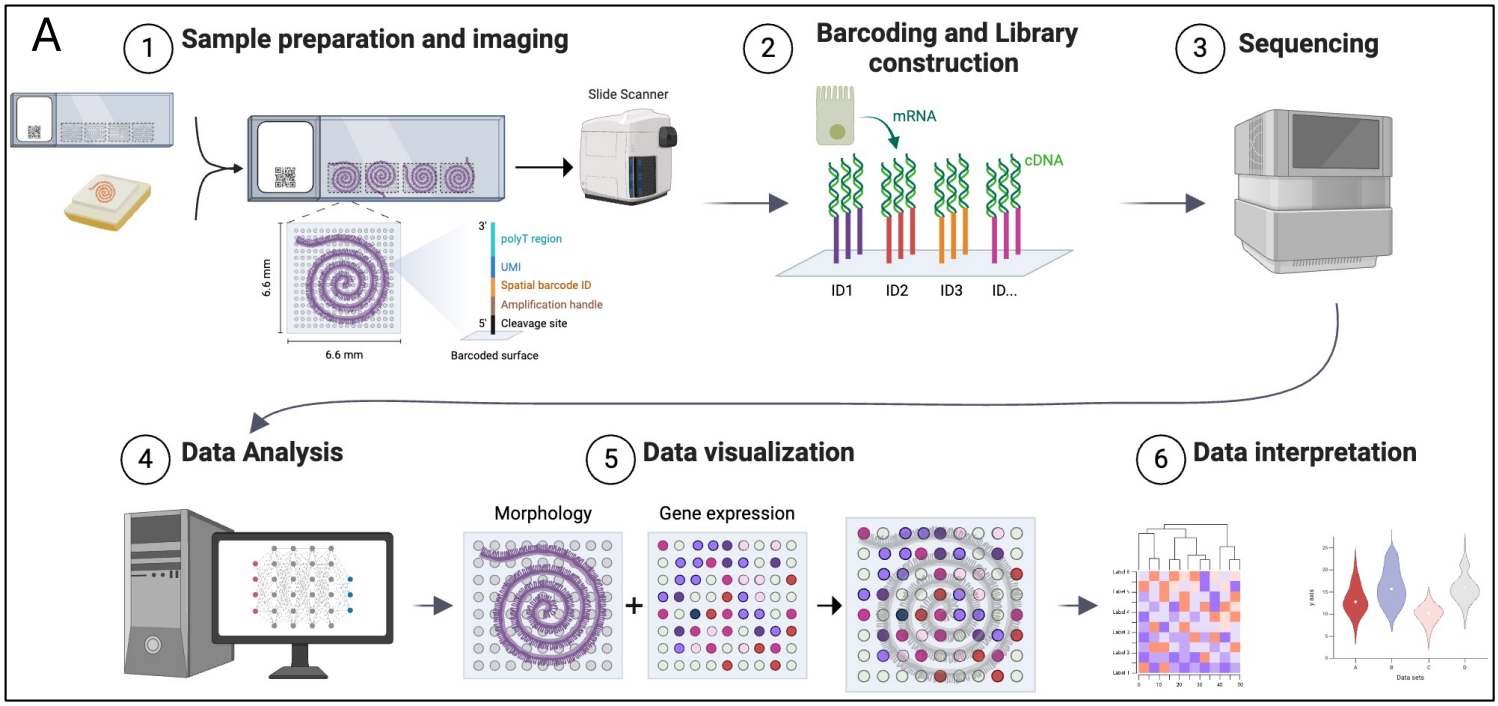
A
1 Sample preparation and imaging
Slide Scanner
6.6 mm
6.6 mm
3'
5'
polyT region
UMI
Spatial barcode ID
Amplification handle
Cleavage site
Barcoded surface
2 Barcoding and Library construction
mRNA
cDNA
ID1
ID2
ID3
ID...
3 Sequencing
4 Data Analysis
5 Data visualization
Morphology
Gene expression
6 Data interpretation

B

C

Crypts
Larva
200µm

D

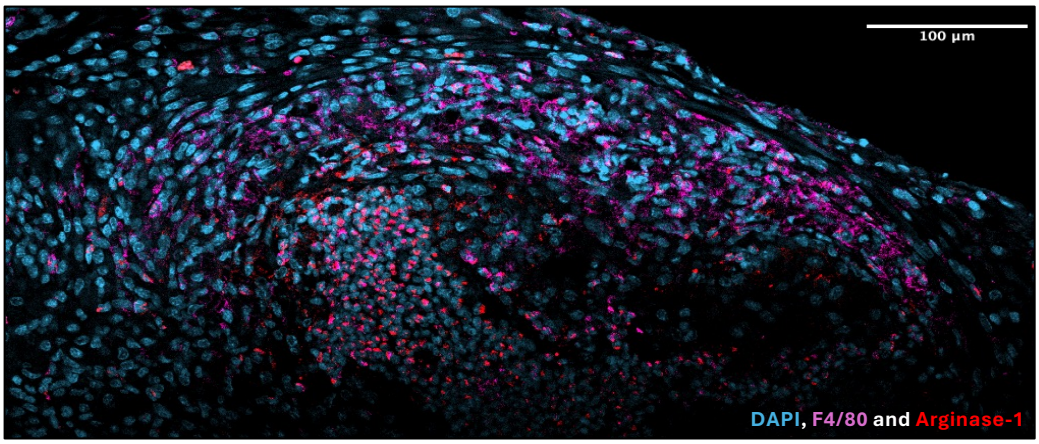
100 µm
DAPI, F4/80 and Arginase-1

788 **Figure Legends**

789 **Figure 1**

790 **Tissue preparation and sequencing**

791 A. Schematics of the experiments: mouse small intestine was processed for gut rolls
792 in Formalin-Fixed Paraffin-Embedded (FFPE) blocks and further spatial
793 transcriptomics with Visium 10X technology.

794 B. Granulomas in the submucosal tissues of *H. polygyrus*-infected C57BL/6 female
795 mice at day 14 following secondary infection.

796 C. Haematoxylin and eosin (H&E)-stained section of typical granuloma containing an
797 *H. polygyrus* larva following primary infection.

798 D. Immunofluorescent staining of granuloma at day 7. Arginase-1-expressing
799 macrophages in the centre of a granuloma, stained with DAPI (cyan), F4/80
800 (violet) and Arginase-1 (red).

Figure 2

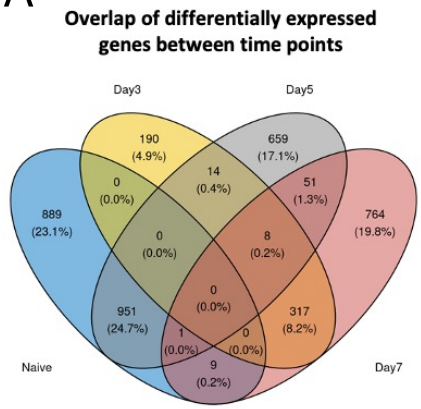
A
Overlap of differentially expressed genes between time points
Day3
Day5
Naive
Day7
190 (4.9%)
659 (17.1%)
889 (23.1%)
764 (19.8%)
0 (0.0%)
14 (0.4%)
51 (1.3%)
0 (0.0%)
8 (0.2%)
0 (0.0%)
951 (24.7%)
317 (8.2%)
1 (0.0%)
0 (0.0%)
9 (0.2%)

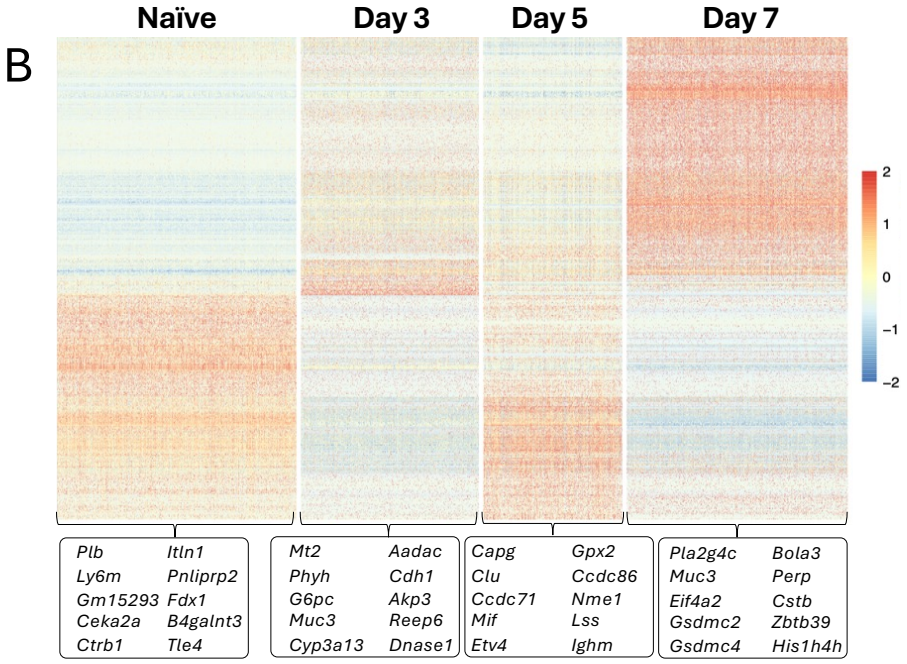
B
Naïve
Day 3
Day 5
Day 7
2
1
0
−1
−2
Plb Itln1
Ly6m Pnliprp2
Gm15293 Fdx1
Ceka2a B4galnt3
Ctrb1 Tle4
Mt2 Aadac
Phyh Cdh1
G6pc Akp3
Muc3 Reep6
Cyp3a13 Dnase1
Capg Gpx2
Clu Ccdc86
Ccdc71 Nme1
Mif Lss
Etv4 Ighm
Pla2g4c Bola3
Muc3 Perp
Eif4a2 Cstb
Gsdmc2 Zbtb39
Gsdmc4 His1h4h

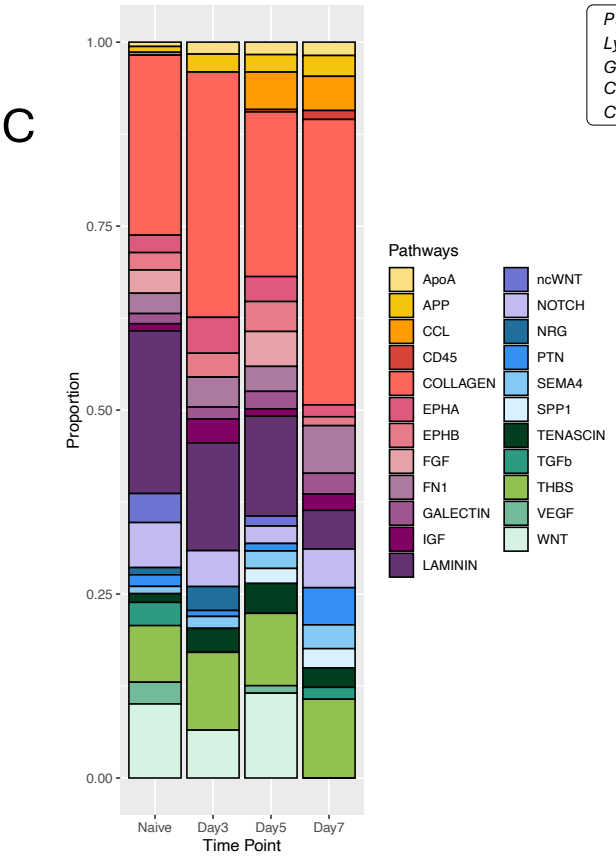
C
Proportion
1.00
0.75
0.50
0.25
0.00
Naive
Day3
Day5
Day7
Time Point
Pathways
ApoA
APP
CCL
CD45
COLLAGEN
EPHA
EPHB
FGF
FN1
GALECTIN
IGF
LAMININ
ncWNT
NOTCH
NRG
PTN
SEMA4
SPP1
TENASCIN
TGFb
THBS
VEGF
WNT

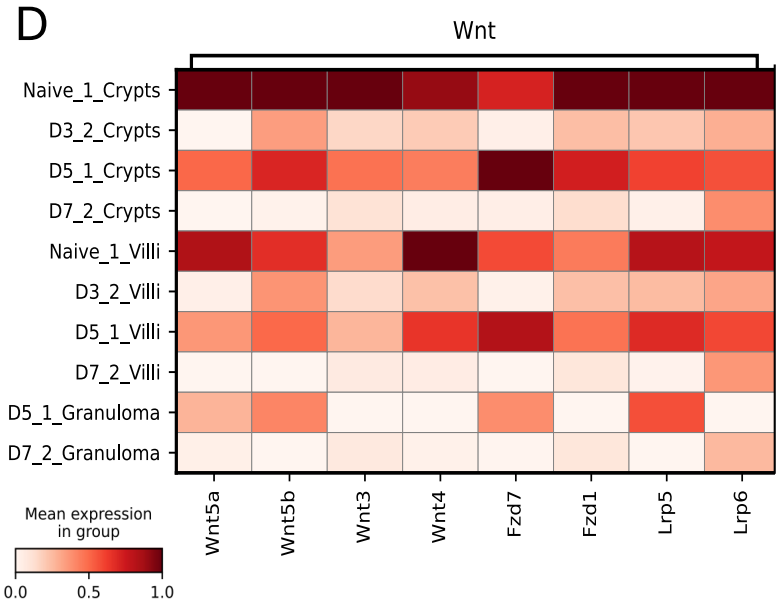
D
Wnt
Naive_1_Crypts
D3_2_Crypts
D5_1_Crypts
D7_2_Crypts
Naive_1_Villi
D3_2_Villi
D5_1_Villi
D7_2_Villi
D5_1_Granuloma
D7_2_Granuloma
Wnt5a
Wnt5b
Wnt3
Wnt4
Fzd7
Fzd1
Lrp5
Lrp6
Mean expression in group
0.0
0.5
1.0

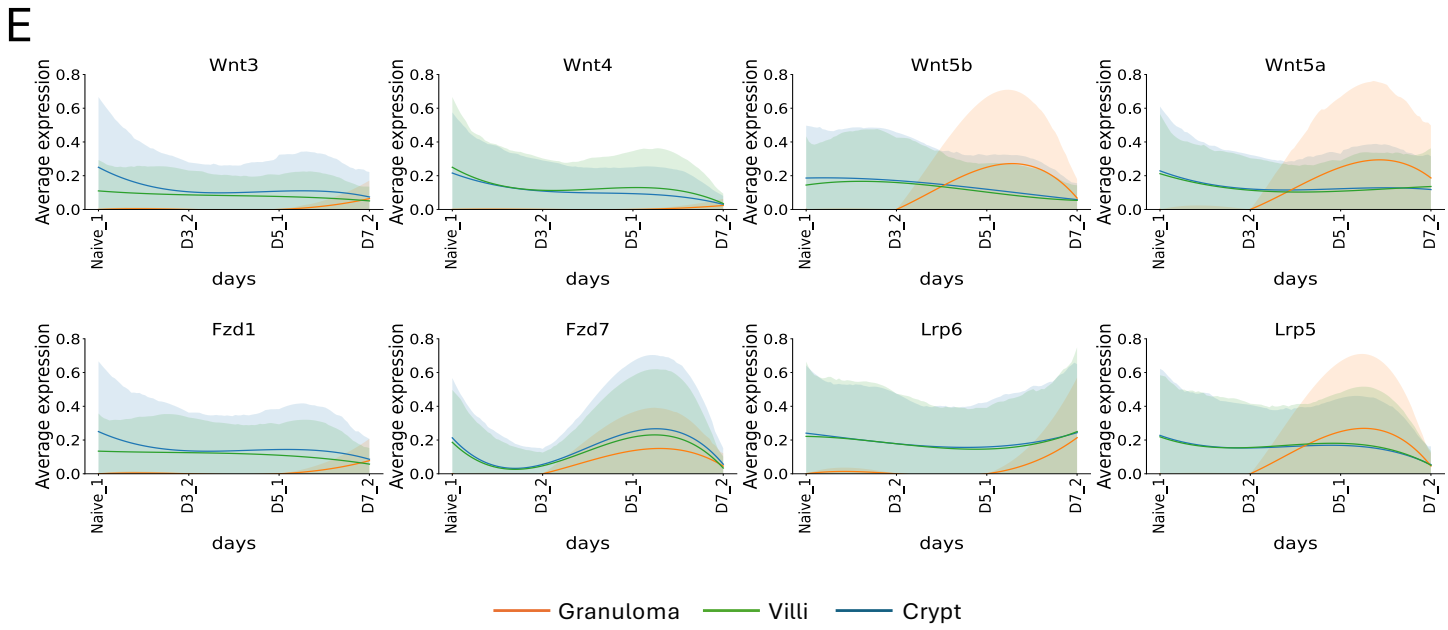
E
Wnt3
Wnt4
Wnt5b
Wnt5a
Fzd1
Fzd7
Lrp6
Lrp5
Average expression
0.0
0.2
0.4
0.6
0.8
Naive_1
D3_2
D5_1
D7_2
days
Granuloma
Villi
Crypt

801 **Figure 2**

802 **Temporal patterns of gene expression during *H. polygyrus* infection in the murine gut**
803 **reveals downregulation of Wnt signalling**

804 A. Venn diagram showing the overlap of differentially expressed genes across each
805 timepoint.

806 B. Heatmap of gene expression in the crypt across all timepoints. The top 10 most
807 highly expressed genes are labelled ordered by their average log fold change
808 values.

809 C. Stacked barplot showing the top interaction pathways at each time point during
810 *H. polygyrus* infection. ApoA, Apolipoproteins; APP, Amyloid Precursor Protein;
811 CCL, Chemokines; CD45, Leukocyte Common Antigen; EPHA/EPHB, Ephrin
812 receptors; FGF, Fibroblast Growth Factor; FN1, Fibronectin; IGF, Insulin-like
813 Growth Factor; ncWNT, non-canonical Wnt; NRG, Neuregulin; PTN, Pleiotophin;
814 SEAMA4, Semaphorin 4; SPP1, Secreted Phosphoprotein/Osteopontin 1; TGFb,
815 Transforming Growth Factor-β, THBS, Thrombospondin; VEGF, Vascular
816 Endothelial Growth Factor; WNT, Wingless/Int-1 (Integration of MMTV).

817 D. Heatmap showing the mean expression of key ligand–receptor interactions in the
818 Wnt signalling and TGF-β pathways across locations and timepoints.

819 E. Average expression of each location of key ligand and receptors involved in the
820 Wnt signalling pathway across time. Lines have been smoothed and fitted using
821 polynomial regression, shaded regions represent confidence intervals for each
822 fitted value. Crypts (blue), Villi (green), Granuloma (orange).

Figure 3

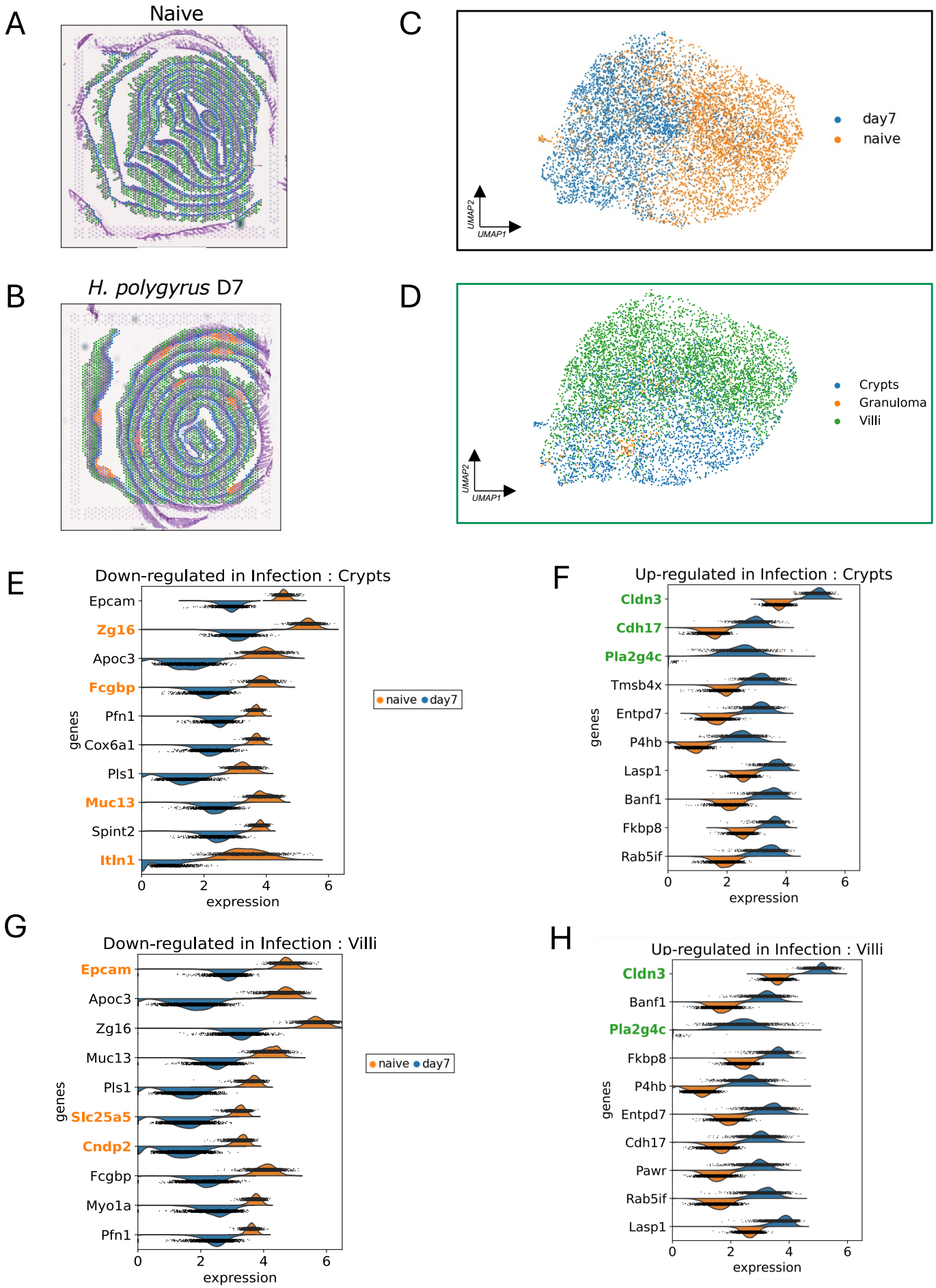
A
Naive
B
H. polygyrus D7
C
day7
naive
UMAP2
UMAP1
D
Crypts
Granuloma
Villi
UMAP2
UMAP1
E
Down-regulated in Infection : Crypts
Epcam
Zg16
Apoc3
Fcgbp
Pfn1
Cox6a1
Pls1
Muc13
Spint2
Itln1
genes
naive
day7
0
2
4
6
expression
F
Up-regulated in Infection : Crypts
Cldn3
Cdh17
Pla2g4c
Tmsb4x
Entpd7
P4hb
Lasp1
Banf1
Fkbp8
Rab5if
genes
0
2
4
6
expression
G
Down-regulated in Infection : Villi
Epcam
Apoc3
Zg16
Muc13
Pls1
Slc25a5
Cndp2
Fcgbp
Myo1a
Pfn1
genes
naive
day7
0
2
4
6
expression
H
Up-regulated in Infection : Villi
Cldn3
Banf1
Pla2g4c
Fkbp8
P4hb
Entpd7
Cdh17
Pawr
Rab5if
Lasp1
genes
0
2
4
6
expression

823 **Figure 3.**

824 **Transcriptomic differences between naïve and 7-day *H. polygyrus* infected mouse**
825 **intestine.**

826 A, B Spatial plots of naïve (**A**) and day 7 *H. polygyrus* infection (**B**) highlighting tissue
827 location clusters.

828 C. UMAP based on Harmony integration of naïve and 7 days post *H. polygyrus*
829 infection Visium datasets coloured by the sample origin of each of the dots.

830 **D.** UMAP based on Harmony integration of naïve and 7 days post *H. polygyrus*
831 infection Visium datasets, coloured by the tissue location of the spots.

832 E-H. Violin plots of the expression of the top 10 differentially expressed genes in naïve
833 and day 7 crypt (**E, F**) and villi (**G, H**). Down-regulated genes are shown in **E** and
834 **G**, up-regulated genes in **F** and **H**, with normalized expression of naïve spots in
835 orange, and day 7 post infection spots in blue.

Figure 4

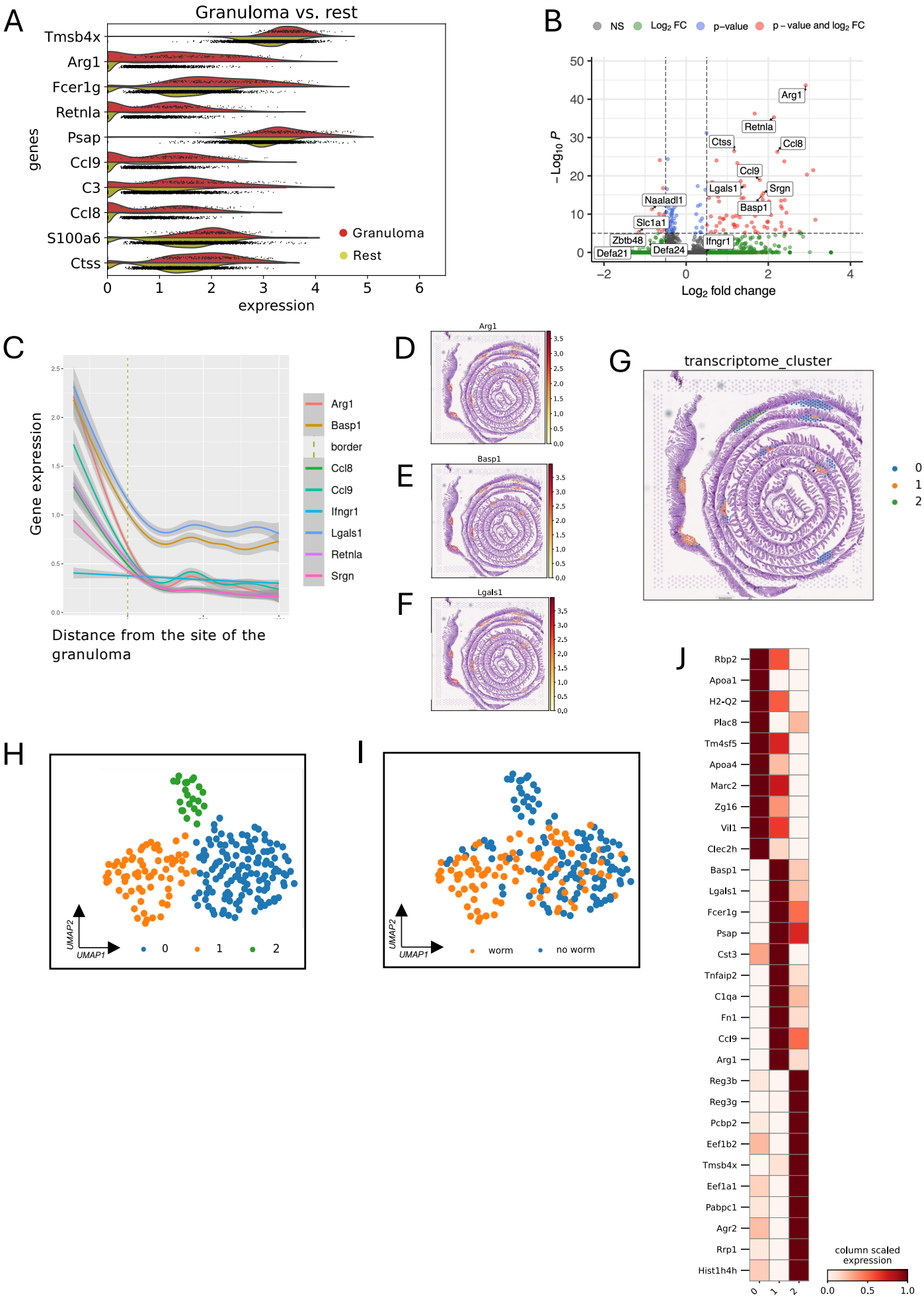
A
Granuloma vs. rest
Tmsb4x
Arg1
Fcer1g
Retnla
Psap
Ccl9
C3
Ccl8
S100a6
Ctss
genes
Granuloma
Rest
expression
B
NS
Log2 FC
p-value
p-value and log2 FC
Arg1
Retnla
Ctss
Ccl8
Ccl9
Lgals1
Srgn
Naaladl1
Basp1
Slc1a1
Zbtb48
Ifngr1
Defa21
Defa24
Log2 fold change
C
Gene expression
Arg1
Basp1
border
Ccl8
Ccl9
Ifngr1
Lgals1
Retnla
Srgn
Distance from the site of the granuloma
D
Arg1
E
Basp1
F
Lgals1
G
transcriptome_cluster
0
1
2
H
UMAP2
UMAP1
0
1
2
I
UMAP2
UMAP1
worm
no worm
J
Rbp2
Apoa1
H2-Q2
Plac8
Tm4sf5
Apoa4
Marc2
Zg16
Vil1
Clec2h
Basp1
Lgals1
Fcer1g
Psap
Cst3
Tnfaip2
C1qa
Fn1
Ccl9
Arg1
Reg3b
Reg3g
Pcbp2
Eef1b2
Tmsb4x
Eef1a1
Pabpc1
Agr2
Rrp1
Hist1h4h
column scaled expression

836 **Figure 4.**

837 **Characterizing transcriptomic signatures of granulomas in the intestine of *H.***
838 ***polygyrus* infected mice.**

839 A. Results of Scanpy marker gene analysis of the top 10 scoring genes for granuloma
840 7 days post *H. polygyrus* infection, displayed as split violin plots of normalized
841 expression values, with red plots for granuloma spots and yellow for non-
842 granuloma spots.

843 B. Volcano plot showing the top 5 up/down regulated genes in the granuloma niche
844 compared to the crypt niche.

845 C. Spatial distribution plot showing the gene expression of the top 8 upregulated
846 genes in the surrounding granuloma niche at d7 of infection. The dotted line
847 denotes the boundary of the spots that are labelled as granuloma but neighbour
848 non-granuloma spots.

849 D-F. Spatial plots showing the gene expression of *Arg1*, *Basp1* and Lgals1 localised
850 exclusively to the granuloma niches.

851 G. Spatial plot of mouse intestine 7 days post infection with *H. polygyrus* with spots
852 coloured by transcriptome-based Leiden clusters.

853 H, I. UMAP of granuloma spots from the mouse intestine 7 days post infection with *H.*
854 *polygyrus* with spots coloured by transcriptome-based Leiden clusters (H) and by
855 absence or presence of *H. polygyrus* based on histological annotation (I).

856 J. Scaled expression of the top 10 gene markers for each granuloma transcriptome-
857 based Leiden cluster.

Figure 5

A

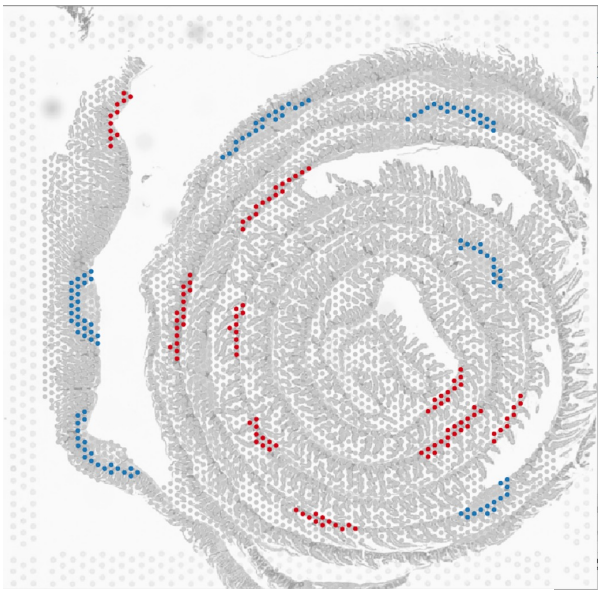

B

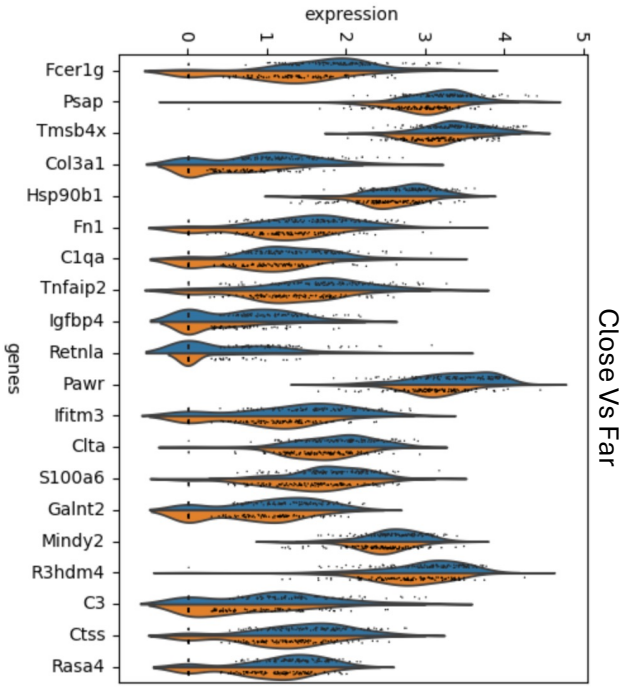

C

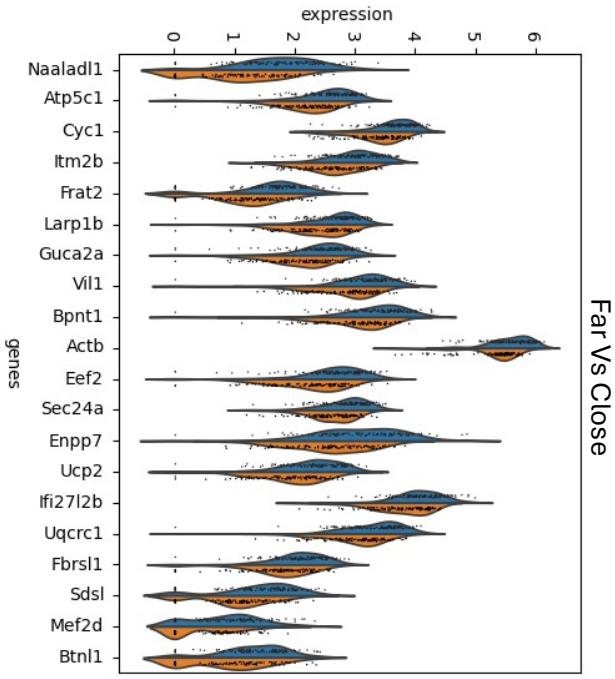

D

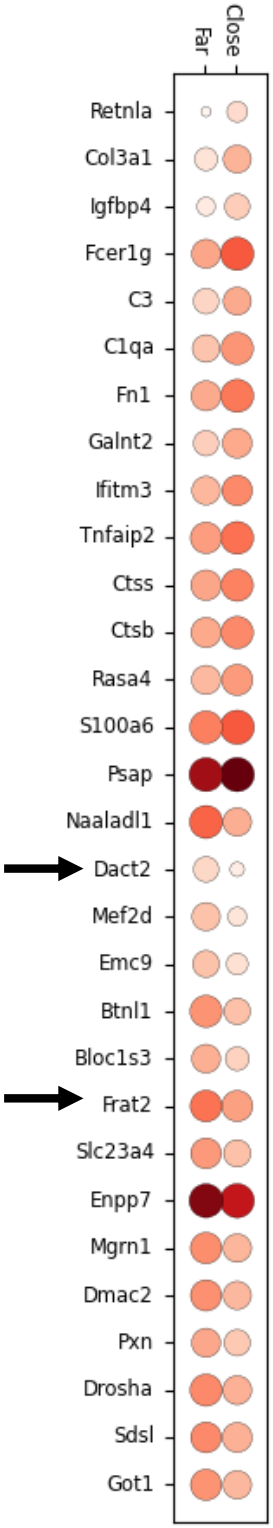

858 **Figure 5**

859 **Proximity to larval parasites modulates epithelial gene expression**

860 A. Designation of crypt areas “close” (blue) or “far (red) from sites of larval
861 encystment.

862 B, C. Violin plots of differential gene expression for top 20 genes upregulated (B) or
863 downregulated (C) in crypts close to parasite locations.

864 D. Dotplot illustrating relative gene expression levels for genes in B and C

Figure 6

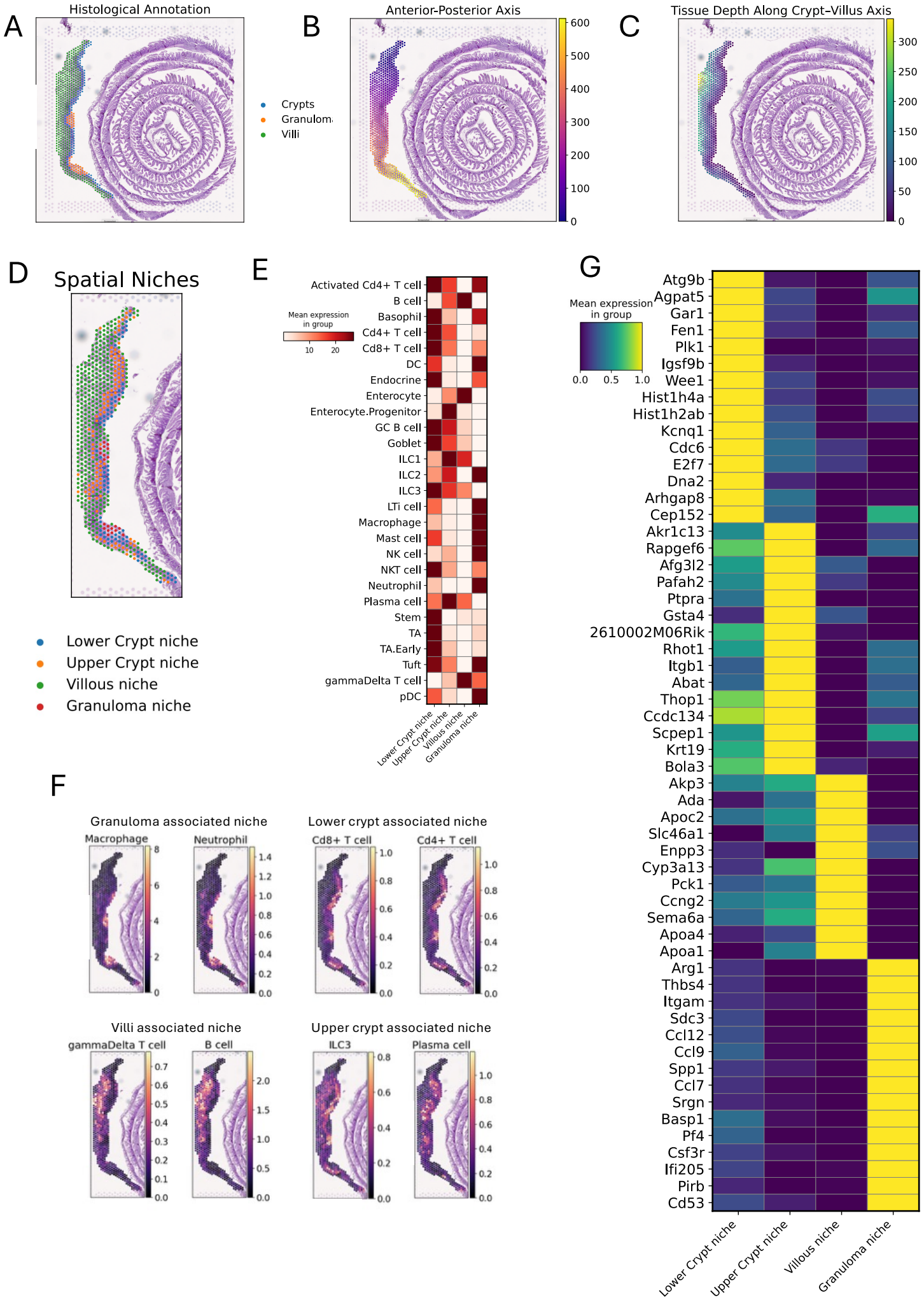
A
Histological Annotation
Crypts
Granulom
Villi
B
Anterior-Posterior Axis
600
500
400
300
200
100
0
C
Tissue Depth Along Crypt–Villus Axis
300
250
200
150
100
50
0
D
Spatial Niches
Lower Crypt niche
Upper Crypt niche
Villous niche
Granuloma niche
E
Mean expression in group
10
20
Activated Cd4+ T cell
B cell
Basophil
Cd4+ T cell
Cd8+ T cell
DC
Endocrine
Enterocyte
Enterocyte.Progenitor
GC B cell
Goblet
ILC1
ILC2
ILC3
LTi cell
Macrophage
Mast cell
NK cell
NKT cell
Neutrophil
Plasma cell
Stem
TA
TA.Early
Tuft
gammaDelta T cell
pDC
Lower Crypt niche
Upper Crypt niche
Villous niche
Granuloma niche
F
Granuloma associated niche
Macrophage
Neutrophil
Lower crypt associated niche
Cd8+ T cell
Cd4+ T cell
Villi associated niche
gammaDelta T cell
B cell
Upper crypt associated niche
ILC3
Plasma cell
G
Mean expression in group
0.0
0.5
1.0
Atg9b
Agpat5
Gar1
Fen1
Plk1
Igsf9b
Wee1
Hist1h4a
Hist1h2ab
Kcnq1
Cdc6
E2f7
Dna2
Arhgap8
Cep152
Akr1c13
Rapgef6
Afg3l2
Pafah2
Ptpra
Gsta4
2610002M06Rik
Rhot1
Itgb1
Abat
Thop1
Ccdc134
Scpep1
Krt19
Bola3
Akp3
Ada
Apoc2
Slc46a1
Enpp3
Cyp3a13
Pck1
Ccng2
Sema6a
Apoa4
Apoa1
Arg1
Thbs4
Itgam
Sdc3
Ccl12
Ccl9
Spp1
Ccl7
Srgn
Basp1
Pf4
Csf3r
Ifi205
Pirb
Cd53
Lower Crypt niche
Upper Crypt niche
Villous niche
Granuloma niche

865 **Figure 6**

866 **Spatial colocalization of cell types within *H. polygyrus* infected mouse intestine.**

867 A. Visium slide of mouse intestine 7 days post *H. polygyrus* coloured by the
868 histological tissue location.

869 B, C. Visium slides of mouse intestine 7 days post *H. polygyrus* showing spots coloured
870 by the recreated length (B) or depth (C) axis.

871 D. Visium slide of mouse intestine 7 days post *H. polygyrus* coloured by spatial
872 niches.

873 E. Heatmap showing the relative mean expression of each cell type signature
874 present in the Xu/Huber reference single cell dataset across each spatial niche.

875 F. Spatial projects of the top 2 predicted cell types in each spatial niche coloured by
876 normalised cell abundance.

877 G. Top 15 highly expressed genes for each spatial niche in the infected intestine.

Figure 7

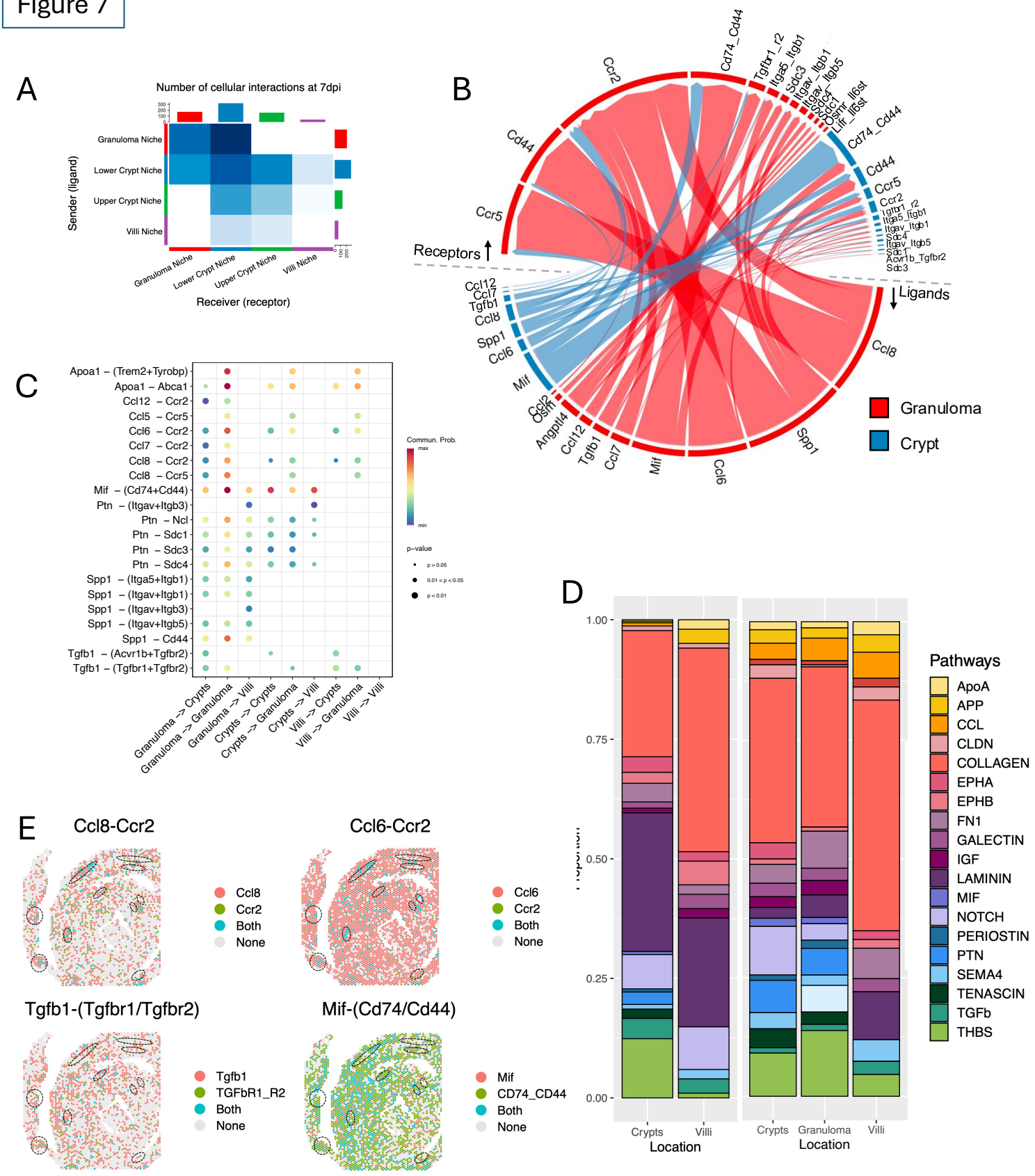
A
Number of cellular interactions at 7dpi
Sender (ligand)
Granuloma Niche
Lower Crypt Niche
Upper Crypt Niche
Villi Niche
Receiver (receptor)
B
Receptors
Ligands
Granuloma
Crypt
C
Apoa1 – (Trem2+Tyrobp)
Apoa1 – Abca1
Ccl12 – Ccr2
Ccl5 – Ccr5
Ccl6 – Ccr2
Ccl7 – Ccr2
Ccl8 – Ccr2
Ccl8 – Ccr5
Mif – (Cd74+Cd44)
Ptn – (Itgav+Itgb3)
Ptn – Ncl
Ptn – Sdc1
Ptn – Sdc3
Ptn – Sdc4
Spp1 – (Itga5+Itgb1)
Spp1 – (Itgav+Itgb1)
Spp1 – (Itgav+Itgb3)
Spp1 – (Itgav+Itgb5)
Spp1 – Cd44
Tgfb1 – (Acvr1b+Tgfbr2)
Tgfb1 – (Tgfbr1+Tgfbr2)
Granuloma -> Crypts
Granuloma -> Granuloma
Granuloma -> Villi
Crypts -> Crypts
Crypts -> Granuloma
Crypts -> Villi
Villi -> Crypts
Villi -> Granuloma
Villi -> Villi
Commun. Prob.
p-value
D
Pathways
ApoA
APP
CCL
CLDN
COLLAGEN
EPHA
EPHB
FN1
GALECTIN
IGF
LAMININ
MIF
NOTCH
PERIOSTIN
PTN
SEMA4
TENASCIN
TGFb
THBS
Crypts
Villi
Location
Crypts
Granuloma
Villi
Location
E
Ccl8-Ccr2
Ccl8
Ccr2
Both
None
Ccl6-Ccr2
Ccl6
Ccr2
Both
None
Tgfb1-(Tgfbr1/Tgfbr2)
Tgfb1
TGFbR1_R2
Both
None
Mif-(Cd74/Cd44)
Mif
CD74_CD44
Both
None

878 **Figure 7: Cellular interactions across spatial niches during *H. polygyrus* infection in**
879 **the murine gut.**
880 A. Heatmap showing the number of ligand-receptor (L-R) interactions inferred by
881 CellChat for each spatial niche at 7 days post infection. Bar plots at top and side
882 show the sum of all interactions.
883 B. Circos plot visualisation showing upregulated ligand and receptor pairs between
884 the granuloma (red) and the lower crypt (blue) niche. Ligands are placed in the
885 lower half and receptors in the upper half, with arrows showing directionality of
886 the interaction.
887 C. Dot plot showing the communication probability of each significant ligand
888 receptor interaction between various spatial niches in the murine gut at 7 days
889 post infection.
890 D. Stacked proportion bar plot showing the interaction pathways associated with
891 each location of the murine intestine day 7 post-infection.
892 E. Spatial projection of key interacting pairs involved between the granuloma and
893 crypt niche during *H. polygyrus* infection, coloured by gene expression.